Dynamically Tunable Light-Matter Interactions in Low-Dimensional Material Integrated Nanophotonics

Sinabu Pumulo

A dissertation

submitted in partial fulfillment of the

requirements for the degree of

Doctor of Philosophy

University of Washington

2026

Reading Committee

Arka Majumdar, Chair

Xiaodong Xu

Arthur Barnard

Program Authorized to Offer Degree:

Materials Science and Engineering

University of Washington

Abstract

Dynamically Tunable Light-Matter Interactions in Low-Dimensional Material Integrated Nanophotonics

Sinabu Pumulo

Chair of the Supervisory Committee:
Xiaodong Xu
Department of Materials Science and Engineering

Due to their small mode volumes and strong electromagnetic field confinement, photonic crystal cavities provide an exceptional platform for enhancing light–matter interactions. These interactions have been extensively investigated using conventional emitters such as quantum dots and crystal defects. More recently, two-dimensional (2D) van der Waals materials, particularly transition metal dichalcogenides (TMDs) and magnetic semiconductors such as Chromium Sulfide Bromide (CrSBr), have emerged as promising emitters owing to their rich excitonic properties, enabling phenomena including exciton-polaritons, enhanced photoluminescence, and single-photon emission. However, integrating 2D materials with nanophotonic cavities remains challenging because fabrication and transfer processes frequently introduce spectral detuning between the emitter and cavity resonance. This mismatch is commonly addressed through iterative fabrication and trial-and-error optimization, limiting reproducibility and scalability.

This dissertation investigates dynamic approaches for overcoming resonance detuning in integrated nanophotonic platforms. It first explores mechanical strain as a means of tuning the optical resonances of WSe_2. Subsequently, we introduce a nondestructive, reversible, and reproducible tuning mechanism to counteract detuning, based on the magnetic properties of CrSBr. This approach addresses several of the limitations associated with strain-based

approaches.

Beyond external tuning mechanisms, this dissertation examines spatial confinement as an additional strategy for tailoring light–matter interactions. In conventional low-dimensional semiconductor systems, including quantum dots, nanowires, and quantum wells, quantum confinement requires dimensions comparable to the exciton Bohr radius, making precise nanoscale fabrication essential. In contrast, exciton-polaritons possess ultralight effective masses and correspondingly large de Broglie wavelengths, enabling quantum confinement within micron-scale potentials that are substantially easier to realize experimentally. By patterning CrSBr, a high refractive index material that support self-hybridized exciton-polaritons, we are able to observe quantum confinement at larger confinement scales.

This dissertation establishes versatile approaches for dynamically tuning and controlling light–matter interactions in low-dimensional material integrated nanophotonic devices.

Contents

List of Figures

Acknowledgments

I will never be able to adequately acknowledge every single person whose contributions have led me to the point of writing this. Still, I'd like to start by thanking my advisors, Arka Majumdar and Xiaodong Xu.

Arka, your support and guidance have been the pillars that held up my graduate experience. Your passion for research, learning, and the people around you has made my graduate school experience feel more fulfilling, even at the hardest times. I could not have wished for a better mentor, wiser professor or greater advocate than you. Having you as a leader has made being a member of the NOISE (Nano Optoelectronic Integrated System Engineering) lab an experience I will forever treasure as both a researcher and a human being.

Thank you, Xiaodong, for taking a chance on me after an impromptu conversation during an MSE virtual visit. Thanks to you, I was able to carry out research in a field that I have grown so fond of while being surrounded by amazing peers who are conducting the most groundbreaking scientific research. Being a member of the Xu lab has exposed me to some of the most interesting physics I have come across, introduced me to some of the most passionate and driven researchers I have ever met, and allowed me to explore a side of science I otherwise never would have. I am extremely grateful for these experiences and will cherish them eternally.

I'd like to also thank all the other members of my doctoral committee, Dr. Arthur Barnard and Dr. Krithika Manohar, whose contributions have been vital in my academic development.

To Dr. Jaime Cardenas and Dr. Brian Kruschwitz from the Institute of Optics thank you for sparking my love for research.

I'd like to acknowledge all the current and previous members of the Xu group for making

the basement of a physics building feel like home. Geoff, thank you for being a great friend and mentor, and for helping me get more comfortable with the more practical elements of research. Jordan, I will always appreciate you for being there for me and supporting me when I was just beginning my journey as a researcher. John, thanks for showing me that research can be both daunting and fun. Jack, I will cherish all the discussions we had and all the times you went out of your way to make me and others feel welcome. Mai, I will miss talking to you about everything from K-pop to CrSBr. I am so happy that we started at the same time and that I managed to leave before having to experience grad school without you lol. I can't wait to see all the amazing things you will do in your career.

I'd also like to thank members of the NOISE group, whose community I am grateful for. To Hannah, I am so lucky to have had you on the same projects as me! I will always be thankful for your mentorship and also for all the talks we had about trash TV shows. Abhinav, Arnab, and Jie, thank you for all your help during my PhD. Chloe, I will miss sharing an office space with you and catching up on life events each Friday.

To my family, I will be forever grateful for your support, which has been instrumental in all my academic endeavors: my parents who supported me and encouraged me to pursue STEM, Gogo and Mbuya for being the most amazing grandparents ever, Aunt Cathy and Uncle Kondwani for being inspirations to me, Taonga for being the best brother and friend, and to all my extended family for their support.

I also want to recognise Rhodes Park School in Lusaka for being the place I developed the most as a person, and all my friends from there: Thandiwe, Cheswa, Maryam, and Lydia, who unfortunately had to experience me during my teenage years! To Kaelyn, Vika, and Jacob you are family to me, and I am so lucky to know you all.

Naomi, I couldn't have survived these years without you. Cade, thank you for being there for me. Adrian, Sidney, McKinley, Ky, Ava, Amirah, Kalliyah, and Hunter, you made life

outside of school so fun, whimsical and special.

Also, the biggest thank you to Kendrick for making this last year the most meaningful to me and for making sure that I have something to smile about every day.

Thank you all :)

Dedication

to Mirriam and Taonga

Chapter 1

Introduction

1.1 Motivation

Light–matter interactions describe the processes by which electromagnetic radiation interacts with matter. These interactions underpin a wide range of optical phenomena including absorption, emission, scattering and nonlinear optical effects. Light-matter interactions form the basis of technologies spanning photovoltaics, optoelectronics, and quantum information science. Understanding and controlling light–matter interactions has therefore remained a central objective in modern physics and engineering.

Advances in nanophotonics have provided powerful tools for manipulating light on sub-wavelength length scales. In particular, nanophotonic cavities and resonators enable strong confinement of electromagnetic fields within small mode volumes, enhancing interactions between light and matter while offering precise control over optical modes. Continued improvements in nanofabrication have led to increasingly reproducible and sophisticated photonic structures, making engineered light–matter interactions more accessible than ever before.

In parallel, the emergence of two-dimensional (2D) van der Waals materials has introduced a new class of optically active materials with exceptional electronic and excitonic properties.

2D materials such as transition metal dichalcogenides and magnetic semiconductors like CrSBr exhibit a diverse range of optical phenomena that are difficult to realize in conventional bulk semiconductors. At the same time, advances in fabrication and transfer techniques have enabled their seamless integration with nanophotonic platforms, creating opportunities to investigate and engineer new regimes of light–matter interactions.

The convergence of nanophotonics and low-dimensional materials has established a rapidly growing field with significant implications for both fundamental science and emerging photonic technologies. This dissertation focuses on the integration of two-dimensional materials with nanophotonic devices, with particular emphasis on developing reliable and reproducible approaches for dynamically tuning light–matter interactions. By addressing key challenges associated with resonance control and optical confinement, this work seeks to advance the realization of robust, tunable nanophotonic platforms based on low-dimensional materials.

1.2 Outline of Dissertation

Chapter 2 provides the scholarly background necessary to understand the work presented in this dissertation, introducing the fundamental concepts, materials, and physical principles that underpin the research.

Chapter 3 explores spatial confinement as a powerful approach for tailoring the optical properties of self-hybridized materials. In particular, the effects of confinement and magnetism on CrSBr are investigated, providing further insight into the versatile optical and magneto-optical properties of this material while offering a novel means of tuning the materials resonance.

Chapter 4 examines mechanical strain as a method for mitigating one of the primary challenges in integrated photonics: spectral detuning between emitters and photonic cavities. By mechanically tuning the optical resonances of WSe_2, this chapter demonstrates a means

of improving resonance matching and achieving more reliable light-matter coupling.

Chapter 5 investigates magnetism in CrSBr as a nondestructive, reversible, and reproducible approach for overcoming resonance detuning. By exploiting the intrinsic magneto-optic properties of CrSBr, this chapter demonstrates a versatile tuning mechanism that addresses a common limitation in integrated 2D material photonics while preserving device integrity.

Chapter 2

Background

2.1 Nanophotonics

The control of the optical properties of materials has been a goal in the scientific community for the past few decades[1,28,29]. This is because of the fascinating developments that continue to arise from the ability to control light waves over ranges of frequencies (wavelength) - perfect reflections, light propagation in only preferred directions, or electromagnetic wave confinement in specific volumes[1]. The development that made this complex prospect realizable was the photonic crystal (PhC). A PhC is a structure of periodic dielectric constant (refractive index). This periodicity in the crystal can create forbidden frequencies in which light of specific frequencies cannot propagate; this is aptly termed the photonic bandgap.

"Bandgap" is a term borrowed from the field of semiconductor physics, where the photonic bandgap parallels the electronic bandgap. This connection allows for a direct association of the PhC with the more familiar concept of crystal structures. Instead of a lattice of atoms or molecules, a PhC has a periodic arrangement of media with dissimilar dielectric functions. When there is a significant difference in the refractive index of the media composing the PhC, light absorption decreases, and the dominant optical phenomena become refraction and reflection. This produces similar effects for photons as the atomic potential does for

electrons. As a result, PhCs can function as low-loss structures, utilizing their photonic band gaps to prevent light of specific frequencies from propagating in certain directions as shown in .

PhCs, similar to crystalline solids, can be classified by their dimensionality and geometry, both of which determine their optical properties and symmetry. One-dimensional (1D) PhCs exhibit periodicity along a single spatial direction, two-dimensional (2D) PhCs are periodic in two directions, and three-dimensional (3D) PhCs possess periodicity in all three dimensions. The dimensionality of a PhC dictates the extent and directionality of its photonic bandgap.

1D PhCs, which exhibit a photonic bandgap only along the direction of periodicity, have been employed for well over a century. A notable example is the Bragg mirror, first described by Lord Rayleigh in 1887, which consists of alternating dielectric layers that reflect a specific range of wavelengths and can localize light through the introduction of structural defects. More recently, 2D PhCs have become the most widely studied and utilized photonic crystal platform. They offer greater flexibility for engineering optical confinement and guiding compared with 1D structures while remaining significantly simpler to design and fabricate than fully 3D PhCs.

When defects are introduced into a PhC, localized optical modes can develop within the photonic bandgap. This occurs because the surrounding periodic structure acts as distributed Bragg reflectors (DBRs), confining light around the defect at specific resonant frequencies. A PhC that supports these localized modes is referred to as a Photonic Crystal Cavity (PCC). The nanoscale dimensions of a PCC enable extremely small mode volumes (V), resulting in enhanced light confinement and strong light-matter interactions. Together with the mode volume, the quality factor (Q) is one of the most important parameters used to characterize a cavity. The quality factor quantifies how efficiently a cavity stores optical energy relative to its losses and is defined as

$$Q = \frac{\omega_0}{\Delta\omega} = \frac{\lambda_0}{\Delta\lambda}, \tag{2.1}$$

where ω_0 is the angular frequency, λ_0 is the wavelength, $\Delta\omega$ and $\Delta\lambda$ are the respective full widths at half maxima (FWHM). High Q cavities exhibit low optical losses, allowing light to remain confined within the cavity for longer times and thereby enhancing light-matter interactions.

The strength of the interaction between an emitter and an optical cavity is characterized by the emitter-cavity coupling strength (g), which scales inversely with the square root of the cavity mode volume,

$$g \propto \frac{1}{\sqrt{V}}, \tag{2.2}$$

Consequently, if all constants remain, reducing the mode volume increases the electric field experienced by an emitter, thereby enhancing the interaction between light and matter.

As previously discussed, nanophotonic devices, such as PCCs, provide a powerful platform for enhancing light-matter interactions through the strong spatial confinement of electromagnetic fields and the resulting small mode volumes[32,34–36,41]. The mode volume, which is a measure of the spatial confinement of the cavity mode, is defined as

$$V = \frac{\int \epsilon(r)|E(r)|^2 d^3r}{max[\epsilon(r)|E(r)|^2]}, \tag{2.3}$$

$\epsilon(r)$ is the position dependent dielectric permittivity, and $E(r)$ is the electric field. A small mode volume is typically within the order of the diffraction limit (λ/n^3).

With both the Q and V defined, it is appropriate to introduce one of the most widely used figures of merit for optical cavities the ratio Q/V. This quantity characterizes a cavity's ability to simultaneously confine light within a small spatial volume while minimizing optical losses, thereby maximizing the interaction between the confined electromagnetic field and nearby emitters. Cavities with a large Q/V ratio allow photons to remain confined for longer periods within highly localized optical modes, increasing the probability of light-

matter interactions.

A high Q/V ratio is directly related to several important cavity quantum electrodynamics (cQED) phenomena. Most notably, it leads to enhanced spontaneous emission through the Purcell effect ($F_P \propto Q/V$), where the local density of optical states is increased, causing emitters to radiate more efficiently into the cavity mode. As the interaction strength between the emitter and the cavity field increases, the system can transition into the strong-coupling regime, where energy is coherently exchanged between light and matter faster than either can dissipate, giving rise to hybrid light-matter states, called polaritons[32,42,43]. Polaritons blend the characteristics of their constituent parts: they have a degree of delocalization gained from the photon, while retaining a mass and a finite scattering cross section inherited from the boson, which can enable non-linear effects and strongly correlated phenomena[32,35–37,40,44]. Furthermore, the enhanced electromagnetic field intensity associated with small mode volumes lowers the optical power required to access nonlinear processes, enabling low-threshold nonlinear effects such as frequency conversion, optical switching, and all-optical modulation. Consequently, maximizing the Q/V ratio is a primary objective in the design of nanophotonic cavities for applications ranging from quantum information processing and cQED to nonlinear and integrated photonics.

2.2 2D Materials

Van der Waals (VdWs) or 2D materials are a class of structures that have strong in-plane covalent bonds but weak interlayer bonding (VdWs interactions). Their weak interlayer bond allows them to be reduced to atomically thin layers through exfoliation. At the atomic level, 2D materials exhibit novel electronic and optical behaviors that are distinct from their bulk counterparts[25]. For instance, Transition Metal Dichalcogenides (TMDs) transition from having an indirect to a direct bandgap in the 2D regime[30].

The stackable nature of VdWs materials enables the formation of an almost limitless variety of heterostructures through layer-by-layer assembly along the out-of-plane direction, without the lattice-matching constraints typically encountered in conventional semiconductor heterostructures[21]. This layered architecture also facilitates their integration with nanophotonic devices, including waveguides and cavities, without any lattice matching conditions. In contrast to conventional emitters, such as quantum dots, large-area 2D flakes can be deterministically transferred onto prefabricated photonic structures with precise spatial alignment and crystallographic orientation. This deterministic integration provides considerable flexibility in device design while enabling efficient spatial overlap between the optical mode and the active material.

These materials are also highly attractive because of their strong interactions with light, which are primarily governed by excitons, composite bosonic quasiparticles consisting of Coulomb bound electron-hole pairs. The reduced dimensionality of 2D materials gives rise to weak dielectric screening, strengthening the Coulomb interaction between electrons and holes and resulting in the formation of tightly bound excitons with large binding energies[?,?]. Consequently, excitonic effects dominate the optical response of many 2D materials and play a fundamental role in a wide range of optoelectronic, spintronic, and valleytronic phenomena[2,8].

The optical properties of 2D materials can be precisely tailored through a variety of external and intrinsic tuning parameters, including the number of layers, mechanical strain, electric and magnetic fields, twist angle in multilayer heterostructures, and temperature. This exceptional tunability provides a versatile platform for engineering light-matter interactions and enables access to a wide range of optical phenomena that are difficult to realize in conventional bulk semiconductors.

Mechanical strain is particularly attractive because the atomic thickness of 2D materials

allows them to sustain large elastic deformations while maintaining excellent mechanical integrity. Their high Young's modulus and, in many cases, strong piezoelectric response enable significant modifications of the electronic band structure and excitonic transitions through relatively small applied strains. Compared with conventional quantum emitters, strain can be introduced in a more controlled and reproducible manner, making it an effective approach for tuning optical resonances.

Applying an electric field provides another powerful means of controlling the optical response through the electro-optic effect, whereby the dielectric function of a material is modified by changes in the carrier density or electronic structure [5].[12] The high carrier mobility and excellent optical properties of many 2D materials make them particularly well suited for electrically tunable optoelectronic devices, including enhanced electroluminescence and electrically controlled light emission[38].

Magnetic field tuning offers an additional degree of control in materials with intrinsic magnetic ordering. Magnetization modifies the electronic band structure and optical selection rules, leading to changes in the optical absorption spectrum as well as the intensity and polarization of emitted or transmitted light. These magneto-optic effects provide a nondestructive mechanism for dynamically tuning light-matter interactions while simultaneously enabling the investigation of spin-dependent optical phenomena[39].

2.2.1 TMDs

Transition Metal Dichalcogenides are 2D materials with a composition of the type MX2, where M represents the transition metal atom (such as Mo or W) and X the chalcogen atom (such as S, Se or Te)[31]. TMDs have the hexagonal 2H lattice when most stable. TMDs were first researched for their 2D physics phenomena after the scientific breakthroughs in the fellow lubricant, graphene[7]. Unlike graphene however, these materials have a direct bandgap at the monolayer, ranging from 1-2ev, and are therefore direct bandgap semiconductors. A huge

reason for the interest in TMDs is their ability to demonstrate strong photoluminescence (PL)[19–24].

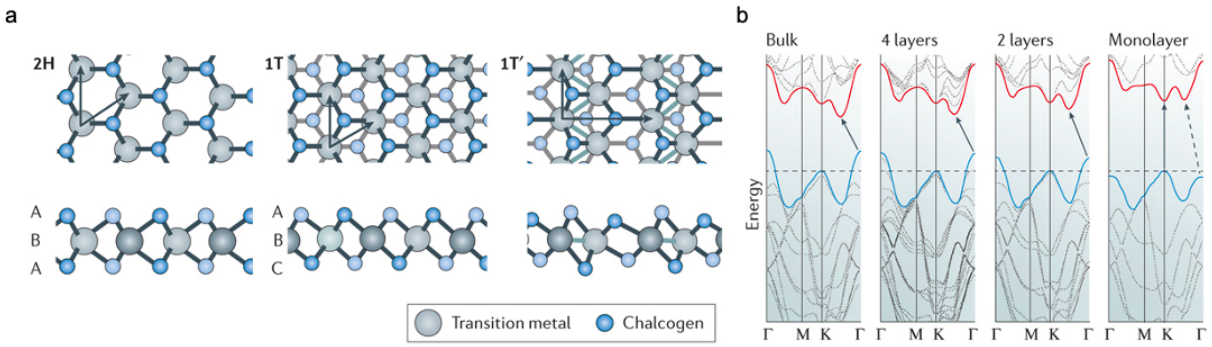

Figure 2.2.1: (a) Schematics of atomic structure of monolayers of TMDs in their trigonal prismatic (2H), distorted octahedral (1T) and dimerized (1T') phases. (b) The band structures of 2H phase MoS_2, calculated for samples of varying thicknesses. Reproduced with permission from: ref. 6 © 2017 Macmillan Publishers Limited

The exact structure of TMDs is a hexagonal honeycomb lattice with two dichalcogenides for every metal atom (Fig. 4a). This means at monolayer, which is often explored, TMDs do not have inversion symmetry (inversion symmetry is broken) leading to some of the novel behavior exhibited by these materials. Particularly the lack of an inversion center at one-layer allows to access to k-valley index degree of freedom[8,21]. In their monolayers, TMDs also have strong spin–orbit coupling which leads to a spin–orbit splitting of hundreds meV in the valence band and a few meV in the conduction band, which allows control of the electron spin by tuning the excitation laser photon energy and handedness[9,24]. Another important property of TMD monolayers is their large exciton binding energy (0.5–1 eV) which, as expected, arises from the reduced dielectric screening relative to the bulk[20–23,33]. This leads to strong and long-lived excitons[21].

Another axis of exploration offered by TMDs, is their capacity to form moiré superlattices. These superlattices can house more excitonic states than their ML counterparts and have the added advantage of having localized excitons at high symmetry points in their lattice as

in Fig. 5; one example of these is the interlayer excitons which form between layers of type II band-aligned TMDs where the electron-hole pairs are confined in two different layers[12–14].

Such localized excitons have been shown to have discrete emission spectrum and single photon generation. Additionally, having localized excitons enhances the potential for light matter coupling - especially when considering the highly localized modes of nanophotonic cavities[10]. The spatially periodic interlayer excitons inherit the spin-valley contrasting properties of the heterobilayer (HBL) components[20–23]. This multitude of exotic properties make them extremely interesting for exploring correlated phases of electrons and coherent spin-photon interfaces through the coupling to a local optical field in a nanocavity[11].

2.2.2 CrSBr

CrSBr is a 2D A-type antiferromagnetic (AFM) direct bandgap semiconductor with a rectangular lattice belonging to the orthorhombic space group Pmmm. As an A-type AFM, CrSBr exhibits in-plane ferromagnetic (FM) ordering and out-of-plane AFM ordering. This magnetic configuration supports two magnon (spin wave) branches, where magnons are quasiparticles corresponding to the collective precession of neighboring magnetic moments[15].

CrSBr undergoes a temperature-dependent magnetic phase transition at its Néel temperature, T_N, which lies between approximately 132-150 K, as shown in Fig. 6c. In bilayer CrSBr, this magnetic transition is accompanied by a pronounced change in the PL spectrum. Since the optical response is dominated by excitonic emission, the observed shift indicates a modification of the excitonic properties across the magnetic phase transition. This provided some of the earliest evidence of coupling between the magnetic ordering and the electronic structure of CrSBr[16].

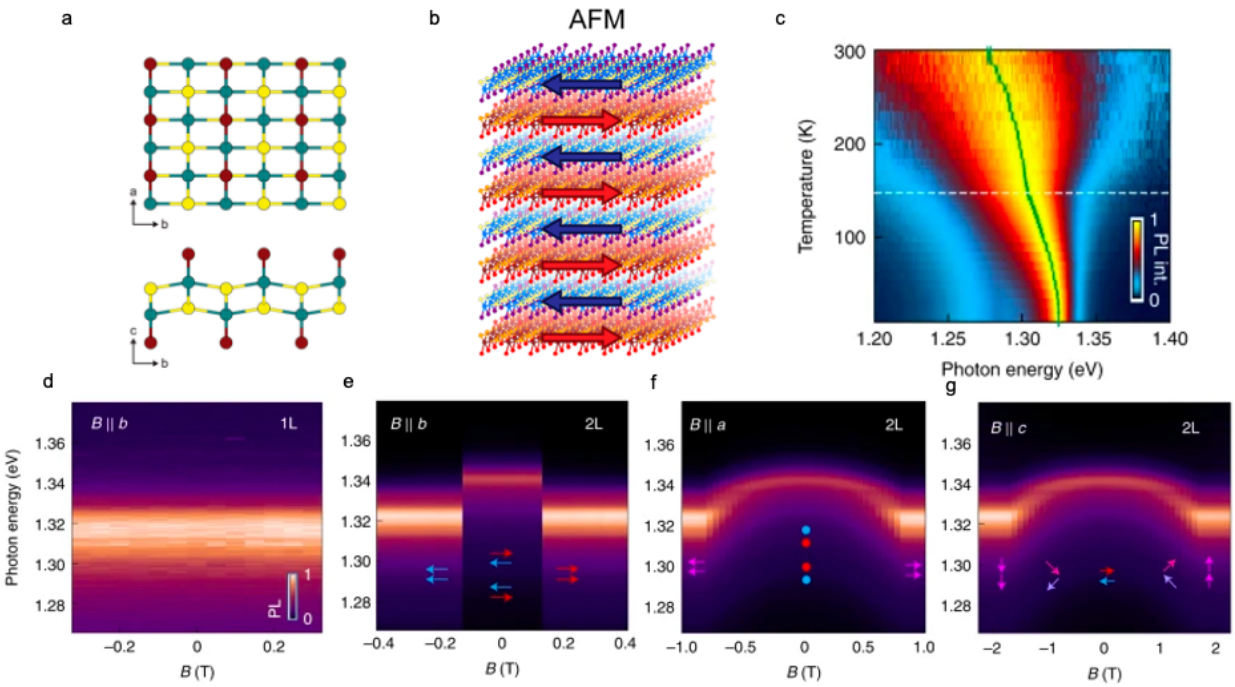

Figure 2.2.2: (a) Crystal structure of CrSBr along c (top) and a (bottom) axes. (b) Structures of AFM phases in bulk CrSBr at zero field. (c) PL spectra from bilayer CrSBr as a function of temperature. (d) Magnetic field dependence of monolayer (1L) PL spectrum with the field oriented along the easy axis. Magnetic field dependence of bilayer (2L) PL spectrum along the intermediate (e), easy (f) and hard axes (g), respectively. Reproduced with permission from: (a) and (b) ref. 15 ©2021; (c-g) ref. 16 © 2021.

The coupling between magnetism and excitons becomes even more apparent under an applied magnetic field. As shown in Fig. 7a, monolayer (ML) CrSBr exhibits negligible changes in its PL spectrum with increasing magnetic field, consistent with its intrinsic FM ground state, where the application of an external field does not alter the magnetic ordering. In contrast, bilayer (BL) CrSBr exhibits an approximately 0.02 eV shift in the PL energy as the magnetic field is increased. At a critical magnetic field, the interlayer spins undergo a spin-flip transition, driving the material from an AFM to an FM state. While this field-induced spin-flip transition is characteristic of A-type AFMs, the accompanying shift in excitonic energy is particularly significant, demonstrating a direct coupling between the magnetic ordering and the excitonic states. This change in excitonic energy originates from interlayer hybridization in the FM state of the bilayer. In the AFM phase, excitons in the two layers are effectively

decoupled. Following the field-induced transition to the FM state, the excitonic states of the two layers hybridize, resulting in the formation of lower-energy hybridized excitonic states and the corresponding reduction in the observed excitonic transition energy.

Adding to its unique properties, CrSBr also hosts self-hybridized EPs[17,45–49]. These arise from the large dielectric contrast between the CrSBr crystal and its surrounding interfaces, typically vacuum and a substrate. In mesoscopic CrSBr flakes, this dielectric mismatch forms a vertically confined Fabry-Pérot (FP) resonator, where the confined optical field strongly couples to the in-plane excitons, giving rise to self-hybridized EPs. Consequently, CrSBr simultaneously functions as both the optical emitter and the resonant cavity supporting the coupled light-matter states. These EPs remain tunable through the application of a magnetic field, resulting in light-matter quasiparticles that are not only hybridized photons and excitons but also are coupled to the magnetic ordering of the crystal through magnons (spin waves)[13,14]

The coexistence of strong excitonic resonances, intrinsic magnetic ordering, and self-hybridized EPs makes CrSBr an exceptional platform for studying magneto-optic phenomena and light-matter interactions. Integrating CrSBr with engineered photonic cavities provides access to polaritonic states with magnetic order and opens opportunities for exploring rich many-body physics[17].

2.3 Methodology

While several experimental techniques are employed throughout this thesis, the core methods are introduced in this section to provide a general understanding of the nanophotonic fabrication processes, material preparation, and device fabrication used in this work.

2.3.1 Photonic Device Fabrication

Photonic crystals are designed differently depending on the device. The initiation of the design process typically involves identifying the fundamental characteristics of the device: wavelength, substrate, mode volumes or quality factor range. Maxwell's equations are the primary tool used in the design. If a similar device already exists, the design process is condensed, requiring only the adjustment of target parameters to match the frequencies under investigation and maximize the quality factor. The simulation of the adjusted design can be employed using several computer programs, including ANSYS Lumerical and Stanford Stratified Structure Solver (S4). If no similar device design is available, a preliminary effort is needed to determine eigenstates and band structures, which can be done with MIT Photonic Bands (MPB). Following the acquisition of the band information, the design can be simulated using the aforementioned software.

On completion of the design, it is exported to a computer-aided design (CAD) layout for use in the electron beam lithography (EBL) process. A wafer or chip of material, typically bare Si, Si/SiO_2, silicon nitride (Si_3N_4), or gallium phosphide (GaP), is used for the device. The wafer is then spin-coated with an electron beam (EB) resist. Common examples of EB resist utilized in this research include polymethyl methacrylate (PMMA) and ZEP-520. The evenly coated wafer is loaded into the EBL device, where the design is patterned onto it by a stream of electrons. Positive resists, like the ones listed prior, have bonds weakened during exposure: once the wafer is in a solvent, the exposed areas will wash off. If the desired structure is composed of the resist, then the nanofabrication ends here. However, the resist can act as an etch mask if needed. In this format, the pattern is directly on the desired material.

For the devices fabricated in this research, some had 2D material that underwent the EBL process, others had material transferred onto the photonic structures, and others had photonic structures transferred onto 2D material. The configuration of the 2D material and

photonic devices depends on the objective of the project and utilizes all techniques previously discussed.

2.3.2 Materials Fabrication

The material fabrication process commences with the growth of bulk crystals. The crystal growing process is not part of the research undertaken, but it should be noted that high-quality crystal is paramount in the fabrication of exceptional devices. Following the acquisition of bulk material, the process of mechanical exfoliation is exercised to obtain atomically thin flakes[25].

The process of mechanical exfoliation starts by placing a flat piece of bulk material onto an adhesive strip, typically Scotch Magic Tape. The tape is then folded onto itself or another piece of tape - to peel the bulk material into thinner layers. Attaining the desired thickness is marked by a distinct optical contrast of the material on the tape. The pieces of tape can subsequently be used to transfer the material onto a substrate. The tape is placed onto the substrate taut to increase yield and prevent air pockets. To avoid fracturing the material, the tape is pressed firmly onto the substrate using a soft medium such as commercially available erasers or Teflon-tipped tweezers. The tape is then peeled off at variable speed depending on the type of material being exfoliated; TMDs require a slow low-angle peel while CrSBr prefers a fast medium-angle peel. The most widely used substrate is silicon (Si) wafers with nanometers thick silicon dioxide (SiO_2) coatings, known colloquially as Si/SiO_2. The reason for the popularity of these wafers is their relatively flat surfaces, large-scale availability owing to the semiconductor industry, and their high adhesion. However, other substrates are used, such as sapphire and quartz, when optical transmission needs to be measured.

The substrate adhesion can be increased by plasma etching using oxygen, reducing hydrocarbon contaminants and allowing a hydrophilic accumulation of charged OH+ which then attract the Van der Waals materials[26]. The adhesion of the material onto the substrate can

also be increased by heating the substrate to 120 C for 2-3 minutes while the tape is on it. The downside to this approach is that it increases tape residue on the substrate and requires the substrate to be cooled off for about 30 minutes after.

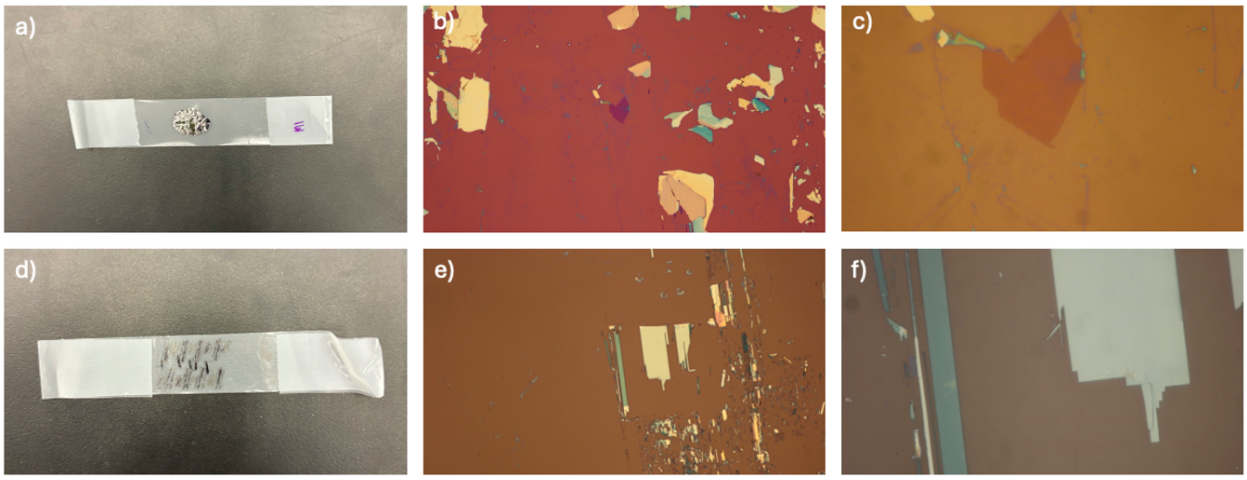

Figure 2.3.1: (a) Images of tape of WSe_2 (b) 20X microscope images of WSe_2 on Si/SiO_2 and (c) 100X microscope image of WSe_2 on Si/SiO_2 (d) Images of tape of CrSBr (b) 20X microscope images of CrSBr on Si/SiO_2 and (c) 100X microscope image of CrSBr on Si/SiO_2

Once on the chip, the material thickness can then be identified using numerous methods. The most utilized in this research is the optical contrast obtained using a brightfield microscope. Optical contrast varies with the interference between the substrate and material - enabling the visual observations through thin film behaviors. These optical effects are reliant on the substrate choice, the material and its thickness. It is possible, using this information, to find the number of layers of a sample using Fresnel equations. Typically, however, for atomically thin material, in the order of 1-3 layers, it is possible and reliable to use visual observations alone to determine the exact number of layers.

In cases where the thickness is unknown or only estimated based on optical contrast, atomic force microscopy (AFM) can also be utilized to determine the near-exact thickness of a sample. This technique allows for observations of the topography of the sample, which gives more information on the level of contaminants such as tape residue or fractures on the

sample.

If a sample of adequately thick 2D material is identified it can either be measured or taken to the next step in fabrication. The decision depends on the type of measurement to be undertaken. Since the research covered is primarily focused on optical measurements, the processes described are catered towards devices made for these experiments.

Material transfer is a fundamental step in the fabrication of 2D material devices. While there are many types of transfer, the core is the same – picking up a flake using a polymer and depositing it onto the desired substrate or sample. Material transfer is how 2D materials can be stacked, as there is no limit to the repetition of this process[27]

This research utilizes the dry transfer method[50]. This process starts by attaching a double-sided tape with a perforation at its center to a glass slide. Following this, a block (2-5mm) of polydimethyl siloxane (PDMS) is placed at the center of the hole. A tape with a hole at its center is covered in polycarbonate (PC) whereafter placed on the glass slide, with the PC-filled hole lining up with the PDMS block. This sandwiched glass slide is called a stamp. The stamp is the vehicle with which the transfer will take place.

The PC dry transfer process starts by placing the sample on a temperature-controlled stage with a live imaging device that can access the area of interest. The stamp should then be mounted on a stage with the PC/PDMS hole in the range of the sample. The heat from the stage will transfer onto the substrate, which allows the polymer to expand when in contact with the sample. The temperature is elevated by 10-30°C to ensure a uniform envelopment of the sample. It is pertinent to avoid delamination while heating, which occurs when temperatures rise beyond the plasticity of the PC. Once the PC expands over the desired region, the temperature is set to a lower figure. At this lower temperature, the polymer begins to contract until it lifts the sample with it. It is possible to continue the process by attaching additional flakes onto the same stamp and even at the same location. The pick-up

process can be repeated to obtain the desired stack. The stamp with the complete stack is placed back into contact with a chip: either one with the bottom of the stack or a clean substrate. In this iteration of the touchdown, however, the heating will be at a temperature past the plasticity of the PC (165°C). The stamp is then elevated, leaving a PC encapsulated sample behind on the chip. For precise transfers, the stage should have vacuum accessibility and be floating, averting vibrations.

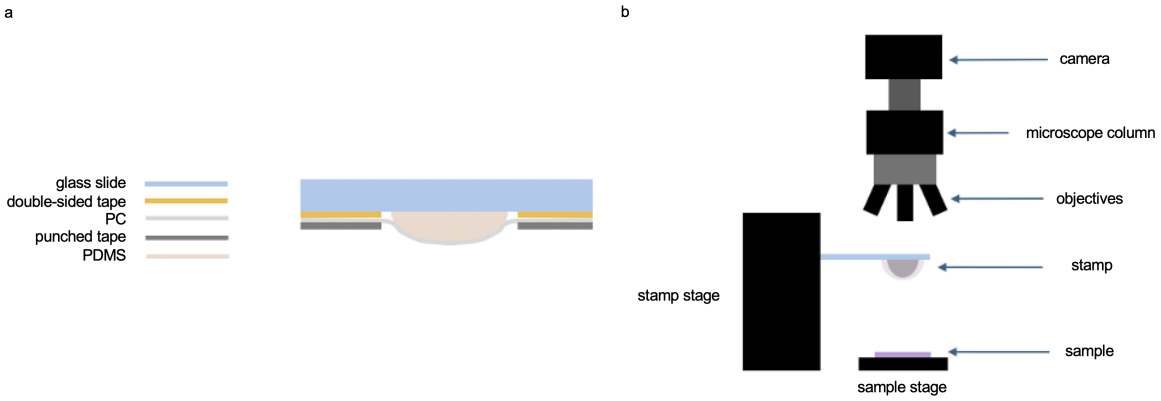

Figure 2.3.2: Representation of: (a) a stamp used in the material transfer process; (b) transfer stage configuration.

The chip will have a detached PC wedge surrounding the sample after the transfer. It must be deposited into a chloroform solvent bath to remove this PC. Following the solvent bath, the chip is washed with isopropanol (IPA) to dissolve any remaining PC. The residual IPA is blown off using a nitrogen gun. Dissolving the PC leaves only the sample on the chip. There is the potential risk of losing the device during this process through fluid behavior when drying or deposition in the bath, so there is an effort made to hamper the sample from drying in the air and limit its movement in the solvent.

By introducing twist angles between material pickups, the construction of twisted hetero bilayers can be achieved using this dry transfer method with relative ease. Additionally, it is understandable why this accurate transfer process allows for 2D materials to be transferred directly and precisely on photonic devices which also have similar substrates and hence are

equally adhesive to 2D materials.

2.3.3 Device Characterization

Characterizing fabricated devices is essential when studying layered materials and nanophotonic structures, as it is often difficult to verify that the intended device has been successfully realized through fabrication alone. Consequently, a range of experimental characterization techniques is employed to probe the structural, optical, and material properties of the devices, with each technique providing complementary information.

Atomic Force Microscopy

Atomic force microscopy (AFM) is a high-resolution scanning probe technique used to determine the dimensions of nanoscale features. In addition to measuring feature sizes, AFM can verify the placement, morphology, and orientation of fabricated structures with nanometer-scale precision.

AFM also plays an important role in device fabrication and optimization. Following the transfer of layered materials, interfacial bubbles and surface contaminants commonly form between the material and the underlying substrate. By operating in contact mode, the AFM tip can be used to mechanically flatten these regions, improving interfacial homogeneity and removing surface debris. This process enhances the quality and reproducibility of fabricated devices.

Photoluminescence Spectroscopy

Photoluminescence (PL) is the spontaneous emission of light from a material following the absorption of electromagnetic radiation. When the excitation energy exceeds the bandgap, photons are absorbed, promoting electrons to higher-energy states and creating electron-hole pairs (excitons). As these excited carriers relax and subsequently recombine radiatively,

photons are emitted with energies characteristic of the material's electronic and excitonic structure. Consequently, PL spectroscopy is a powerful and widely used technique for probing the optical and electronic properties of materials, providing information on parameters such as the bandgap, excitonic transitions, defect states, and material quality.

Reflectance Spectroscopy

Reflectance spectroscopy is a characterization technique used to probe the optical properties of a material by measuring the light reflected from its surface. A broadband light source is directed onto the sample, where specific optical transitions absorb photons at characteristic energies. The remaining light is reflected and collected, producing a spectrum that contains information about the electronic and excitonic states of the material. Unlike PL, reflectance spectroscopy can probe both emissive and non-emissive optical transitions, including dark excitonic states through their influence on the material's optical response.

Because the measured signal contains contributions from both the sample and the surrounding optical system, a background spectrum is first acquired and used to correct the measured reflectance. In this work, differential reflectance is employed, in which the background-corrected signal is normalized by the background reflectance. This normalization suppresses residual background features and enhances the spectral contrast of the optical transitions, providing a more sensitive measurement of the material's electronic and excitonic resonances.

2.4 Bibliography

1. J. D. Joannapoulos, S. G. Johnson, J. N. Winn, R. D. Meade, Photonic Crystals, Vol. 2 (Eds:), Princeton University Press, Princeton, New Jersey 2008

2. S. Latini, E. Ronca, U. D. Giovannini, H. Hübener, A. Rubio, Cavity Control of Excitons in Two-Dimensional Materials, Nano Lett. 2019, 19, 3473-3479

3. A. Ramasubramaniam, Large Excitonic Effects in Monolayers of Molybdenum and Tungsten Dichalcogenides, Phys. Rev. B: Condens. Matter Mater. Phys. 2012, 86, 115409.

4. P. Cudazzo, I. V. Tokatly, A. Rubio, Dielectric Screening in Two-Dimensional Insulators: Implications for Excitonic and Impurity States in Graphane, Phys. Rev. B: Condens. Matter Mater. Phys. 2011, 84, 085406.

5. Q. Ma, G. Ren, K. Xu, J. Z. Ou, Tunable Optical Properties of 2D Materials and Their Applications, Adv. Optical Mater. 2020, 2001313

6. S. Manzeli, D. Ovchinnikov, D. Pasquier, 2D transition metal dichalcogenides, Nat Rev Mater 2017, 33

7. Q. H. Wang, K. Kalantar-Zadeh, A. Kis, J. N. Coleman, M. S. Strano, Electronics and optoelectronics of two-dimensional transition metal dichalcogenides, Nature Nanotechnology 2012, 7, 669-712

8. T. Cao, G. Wang, W. Han, H. Ye, C. Zhu, J. Shi, Q. Niu, P. Tan, E. Wang, B. Liu, J. Feng, Valley-selective circular dichroism of monolayer molybdenum disulphide, Nature Commun. 2012, 3, 887

9. J. A. Reyes-Retanaa, F. Cervantes-Sodi, Spin-orbital effects in metal-dichalcogenide semiconducting monolayers, Sci Rep. 2016; 6: 24093.

10. L. Zhang, F. Wu, S. Hou, Z. Zhang, Y. H. Chou, K. Watanabe, T. Taniguchi, S. R. Forrest, H. Deng, Van der Waals heterostructure polaritons with moiré-induced nonlinearity, Nature 2021, 591, 61-65

11. C. Qian, M. Troue, J. Figueiredo, P. Soubelet, V. Villafañe, J. Beierlein, S. Klembt, A. V. Stier, S. Höfling, A. W. Holleitner, J. J. Finley, Lasing of Moire Trapped MoSe2/WSe2 Interlayer Excitons Coupled to a Nanocavity, Science Advances 2024, 10

12. F. Mahdikhanysarvejahany, D. N. Shanks, M. Klein, Q. Wang, M. R. Koehler, D. G. Mandrus, T. Taniguchi, K. Watanabe, O. L. A. Monti, B. J. LeRoy, and J. R. Schaibley, Localized interlayer excitons in mose2–wse2 heterostructures without a moiré potential, Nat. Commun 2022, 13, 5354

13. P. Rivera, J. R. Schaibley, A. M. Jones, J. S. Ross, S. Wu, G. Aivazian, P. Klement, K. Seyler, G. Clark, N. J. Ghimire, J. Yan, D. G. Mandrus, W. Yao, and X. Xu, Observation of long-lived interlayer excitons in monolayer mose2–wse2 heterostructures, Nat. Commun 2015, 6, 6242

14. S. Wu, S. Buckley, J. R. Schaibley, L. Feng, J. Yan, D. G. Mandrus, F. Hatami, W. Yao, J. Vučkovíc, A. Majumdar, and X. Xu, Monolayer semiconductor nanocavity lasers with ultralow thresholds, Nature 2015, 520, 69

15. K. Lee, A. H. Dismukes, E. J. Telford, R. A. Wiscons, J. Wang, X. Xu, C. Nuckolls, C. R. Dean, X. Roy, and X. Zhu, Magnetic Order and Symmetry in the 2D Semiconductor CrSBr, Nano Lett. 2021, 21, 35113517

16. N. P. Wilson, K. Lee, J. Cenker, K. Xie, A. H. Dismukes, E. J. Telford, J. Fonseca, S. Sivakumar, C. Dean, T. Cao, X. Roy, X. Xu, X. Zhu, Interlayer electronic coupling on demand in a 2D magnetic semiconductor, Nature Materials 2021, 20, 1657-1662

17. T. Wang, D. Zhang, S. Yang, Z. Lin, Q. Chen, J. Yang, Q. Gong, Z. Chen, Y. Ye, W. Liu, Magnetically-dressed CrSBr exciton- polaritons in ultrastrong coupling regime, Nature Communications 2023, 14:5966

18. Q. Li, X. Xie, A. Alfrey, C. W. Beach, N. McLellan, Y. Lu, J. Hu, W. Liu, N. Dhale, B. Lv, L. Zhao, K. Sun, H. Deng, Magnetic Exciton-Polariton with Strongly Coupled Atomic and Photonic Anisotropies, arXiv:2306.11265

19. T. Mueller, E. Malic, Exciton physics and device application of two-dimensional transition metal dichalcogenide semiconductors, npj 2D Mater. Appl. 2018, 2, 29.

20. K. F. Mak, J. Shan, Photonics and optoelectronics of 2D semiconductor transition metal dichalcogenides, Nature Photonics 2016, 10, 216-226

21. F. Xia, H. Wang, D. Xiao, M. Dubey, A. Ramasubramaniam, Two-dimensional material nanophotonics, Nature Photonics 2014, 8, 899-907

22. C. Zhang, A. Johnson, C. L. Hsu, L. J. Li, C. K. Shih, Direct imaging of band profile in single layer MoS2 on graphite: Quasiparticle energy gap, metallic edge states and edge band bending. Nano Lett. 2014, 14, 2243–2247

23. A. Chernikov, T. C. Berkelbach, H. M. Hill, A. Rigosi, Y. Li, B. Aslan, D. R. Reichman, M. S. Hybertsen, T. F. Heinz, Exciton Binding Energy and Nonhydrogenic Rydberg Series in Monolayer WS2, Phys. Rev. Lett. 2014, 113, 076802

24. G. Sallen, L. Bouet, X. Marie, G. Wang, C. R. Zhu, W. P. Han, Y. Lu, P. H. Tan, T. Amand, B. L. Liu, B. Urbaszek, Robust optical emission polarization in MoS2 monolayers through selective valley excitation, Phys. Rev. B 2014, 86, 081301(R); Erratum Phys. Rev. B 2014, 89, 079903

25. K. S. Novoselov, A. K. Geim, S. V. Morozov, D. Jiang, Y. Zhang, S. V. Dubonos, I. V. Grigorieva, A. A. Firsov, Electric Field Effect in Atomically Thin Carbon Films, Science 2004, 306, 5696

26. Y. Huang, E. Sutter, N. N. Shi, J. Zheng, T. Yang, D. Englund, H. J. Gao, P. Sutter, Reliable Exfoliation of Large-Area High-Quality Flakes of Graphene and Other Two-Dimensional Materials, ACS Nano 2015, 9, 11, 10612–10620

27. R. Frisenda, E. N. Moratalla, P. Gant, D. P. D. Lara, P. J. Herrero, R. V. Gorbachev, A. C. Gomez, Recent progress in the assembly of nanodevices and van der Waals heterostructures by deterministic placement of 2D materials, Chem. Soc. Rev. 2018, 47, 53-68

28. S. John, Strong localization of photons in certain disordered dielectric superlattices, Phys. Rev. Lett. 1987, 58, 2486

29. E. Yablonovitch, Inhibited Spontaneous Emission in Solid-State Physics and Electronics, Phys. Rev. Lett. 1987, 58, 2059

30. A. Splendiani, L. Sun, Y. Zhang, T. Li, J. Kim, C. Y. Chim, G. Galli, F. Wang, Emerging Photoluminescence in Monolayer MoS2, Nano Lett. 2010, 10, 4, 1271–1275

31. Z. Y. Zhu, Y. C. Cheng, and U. Schwingenschlögl, Giant spin-orbit-induced spin splitting in two-dimensional transition-metal dichalcogenide semiconductors, Phys. Rev. B 2011, 84, 153402

32. S. Latini, E. Ronca, U. D. Giovannini, H. Hübener, A. Rubio, Cavity Control of Excitons in Two-Dimensional Materials, Nano Letters 2019, 19, 6

33. A. Ramasubramaniam, Large excitonic effects in monolayers of molybdenum and tungsten dichalcogenides, Phys. Rev. B 2012, 86, 115409

34. L. C. Flatten, Z. He, D. M. Coles, A. A. P. Trichet, A. W. Powell, R. A. Taylor, J. H. Warner, J. M. Smith, Room-temperature exciton-polaritons with two-dimensional WS2, Sci Rep 6 2016, 33134

35. L. S. Dang, D. Heger, R. André, F. Bœuf, R. Romestain, Stimulation of Polariton Photoluminescence in Semiconductor Microcavity, Phys. Rev. Lett. 1998, 81, 3920

36. T. Chervy, S. Azzini, E. Lorchat, S. Wang, Y. Gorodetski, J. A. Hutchison, S. Berciaud, T. W. Ebbesen, C. Gene, Room Temperature Chiral Coupling of Valley Excitons with Spin-Momentum Locked Surface Plasmons, ACS Photonics 2018, 5, 4, 1281–1287

37. J. Kasprzak, M. Richard, S. Kundermann, A. Baas, P. Jeambrun, J. M. J. Keeling, F. M. Marchetti, M. H. Szymańska, R. André, J. L. Staehli, V. Savona, P. B. Littlewood, B. Deveaud, L. S. Dang, Bose–Einstein condensation of exciton polaritons, Nature 2006, 443, 409–414

38. W. Jie, Z. Yang, G. Bai, J. Hao, Luminescence in 2D Materials and van der Waals Heterostructures, Advanced Opt. Mat. 2018, 6, 10, 1701296

39. Y. J. Zhang, T. Oka, R. Suzuki, J. T. Ye, Y. Iwasa, Electrically Switchable Chiral Light-Emitting Transistor, Science 2014, 344, 6185, 725-728

40. Y. Chen, S. Miao, T. Wang, D. Zhong, C. Chow, J. Whitehead, X. Xu, S. Shi, A. Majumdar, Metasurface Integrated Monolayer Exciton Polariton, Nano Letters 2020, 20 (7), 5292-5300

41. S. M. Thon, M. T. Rakher, H. Kim, J. Gudat, W. T. M. Irvine, P. M. Petroff, D. Bouwmeester, Strong coupling through optical positioning of a quantum dot in a photonic crystal cavity, Appl. Phys. Lett. 2009, 94, 111115

42. C.Weisbuch, M.Nishioka, A.Ishikawa, Y.Arakawa, Observation of the coupled exciton-photon mode splitting in a semiconductor quantum microcavity, Phys. Rev. Lett. 1992,69, 3314

43. J. J. Hopfield, "Theory of the contribution of excitons to the complex dielectric constant of crystals," Phys. Rev. 1958, 112 1555

44. S. Christopoulos, G. Baldassarri Höger von Högersthal, A.J.D. Grundy, P. G. Lagoudakis, A. V. Kavokin, and J. J. Baumberg, Room-temperature polariton lasing in semiconductor microcavities, Phys. Rev. Lett. 2007, 98 126405

45. Y. Akahane, T. Asano, B. S. Song, S. Noda, High-Q photonic nanocavity in a two-dimensional photonic crystal, Nature 2003, 425

46. Dirnberger, F., Quan, J., Bushati, R. et al. Magneto-optics in a van der Waals magnet tuned by self-hybridized polaritons. Nature 620, 533–537 (2023).

47. Canales, A., Baranov, D. G., Antosiewicz, T. J. Shegai, T. Abundance of cavity-free polaritonic states in resonant materials and nanostructures. J. Chem. Phys. 154, 024701 (2021).

48. Demir, A.K., Nessi, L., Vaidya, S. et al. Tunable nanophotonic devices and cavities based on a two-dimensional magnet. Nat. Photon. (2025).

49. Weber, T. et al. Intrinsic strong light–matter coupling with self-hybridized bound states in the continuum in van der Waals metasurfaces. Nat. Mater. 22, 970–976 (2023)

50. P. J. Zomer;, M. H. D. Guimarães, J. C. Brant, N. Tombros, B. J. van Wees, Fast pick up technique for high quality heterostructures of bilayer graphene and hexagonal boron nitride, Appl. Phys. Lett. 2014, 105, 013101

Chapter 3

Magnetically Coupled Exciton-Polariton Quantum Boxes in CrSBr

This chapter contains contents from a manuscript that is currently under review for publication. The text has been adapted for inclusion in this dissertation: **S. Pumulo**, J. Fang, A. Kala, G. S. J. Nath, Z. Zhou, M. Nguyen, D. G. Chica, X. Roy, J. Barlow, X. Xu, A. Majumdar," Magnetically Coupled Exciton-Polariton Quantum Boxes in CrSBr," under review.

3.1 Abstract

Spatial confinement is a powerful tool for tailoring low-dimensional systems by enabling quantum structures with size-quantized excitonic states. However, attaining this requires nanoscale confinement comparable to the exciton Bohr radius, making precise control challenging. In contrast, exciton-polaritons exhibit quantum confinement even under µm-scale spatial confinement due to their ultralight effective masses and correspondingly µm-scale de Broglie wavelengths. Here, we realize polariton quantum boxes in the van der Waals magnet

CrSBr, patterned into nanodisks, and report a pronounced polariton energy blueshift of up to 6.4 meV with increasing spatial confinement. Additionally, confined CrSBr polaritons inherit magneto-optical characteristics from their excitonic component, allowing us to control polariton energy with an external magnetic field. With the multi-dimensional design freedom spanning geometrical, optical, and magnetic tunability, our results establish CrSBr polariton quantum boxes as a compelling quantum platform and point towards the exploration of novel magnon behaviors under quantization.

3.2 Introduction

Light-matter interactions describe the coupling between electromagnetic fields (photons) and material excitations such as excitons, phonons, and magnons. Achieving strong coupling between these systems enables coherent energy exchange and is the cornerstone in advancements in optical communication, information storage, quantum technologies, integrated photonics, spintronics, and other emerging fields. Exciton-polaritons (EPs) represent a quintessential class of strongly coupled light-matter states; formed through the coherent interaction between cavity photons and semiconductor excitons, EP are typically evidenced by Rabi splitting.

While excitons possess effective masses on the order of 0.1 m_e, their hybrid light-matter counterparts, EPs, exhibit dramatically lighter effective masses in the range of $10^{-5} - 10^{-4}$ m_e[1]. Such ultralow masses yield micrometer-scale thermal de Broglie wavelengths ($\lambda_{th} = \sqrt{\frac{2\pi\hbar^2}{m_{eff}\kappa_B T}}$) at cryogenic temperatures, thereby facilitating the observation of quantum-confinement phenomena within submicron-scale confinement dimensions. $\hbar$ is Planck's constant, m_{eff} is the effective mass of the particle, κ_B is the Boltzmann constant, and T is the absolute temperature. It can be readily observed that reduction in m_{eff} results in an increase in λ_{th}.

Magnetism offers a powerful avenue for probing and controlling the properties of two-dimensional (2D) van der Waals materials[3,18–21]. CrSBr, a semiconducting layered A-type antiferromagnet[24] with in-plane ferromagnetic (FM) and out-of-plane antiferromagnetic (AFM) coupling, serves as a compelling system for exploring the interplay between magnetism and optical response. Below its Néel temperature (132 K)[3], application of a magnetic field beyond the critical field results in a transition from AFM to FM ordering. Correspondingly, excitonic resonance exhibits a red-shift, signifying magneto-optical coupling. Adding to its intrigue, CrSBr also hosts self-hybridized EP[4,5,22,23,28] arising from the large dielectric contrast between the crystal and its interfaces (typically vacuum and substrate). For a thin film of CrSBr crystal, this large dielectric contrast creates a vertically confined Fabry Pérot (FP) resonator, where the highly confined optical near field strongly interacts with the in-plane excitons in CrSBr and forms EPs. This allows the crystal to behave as both an emitter and a sort of self-sustaining FP cavity. Moreover, these EP modes are themselves tunable by magnetic field, enabling a strongly coupled light-matter quasiparticle that is simultaneously coupled to the material's magnetic ordering via magnons (spin waves)[25,26]. This intersection of exciton-magnon coupling and exciton-photon coupling leverages CrSBr as a dynamic candidate for light-matter studies and offers a unique platform for quantum photonics and spintronic applications.

Here, by patterning thin films of CrSBr into cylindrical nanodisks of varying radii, we show that self-hybridized EPs undergo a pronounced energy blue shift with increasing lateral confinement, effectively realizing EP quantum boxes. Remarkably, compared with other 2D material nanodisks[6], CrSBr requires far less geometric confinement to achieve shifts of similar magnitude, an effect attributed to the exceptionally light effective mass of its EPs and the resulting enhancement of their confinement sensitivity. Electromagnetic simulations based on Maxwell's equations reproduce the optical mode structure and confirm the hybrid light-matter character of the resonances, ruling out purely excitonic or photonic origins. Beyond the confinement driven energy control, the persistence of magneto-optical coupling

introduces a complementary degree of freedom, enabling simultaneous tuning of the hybrid mode energy through both structural and magnetic parameters.

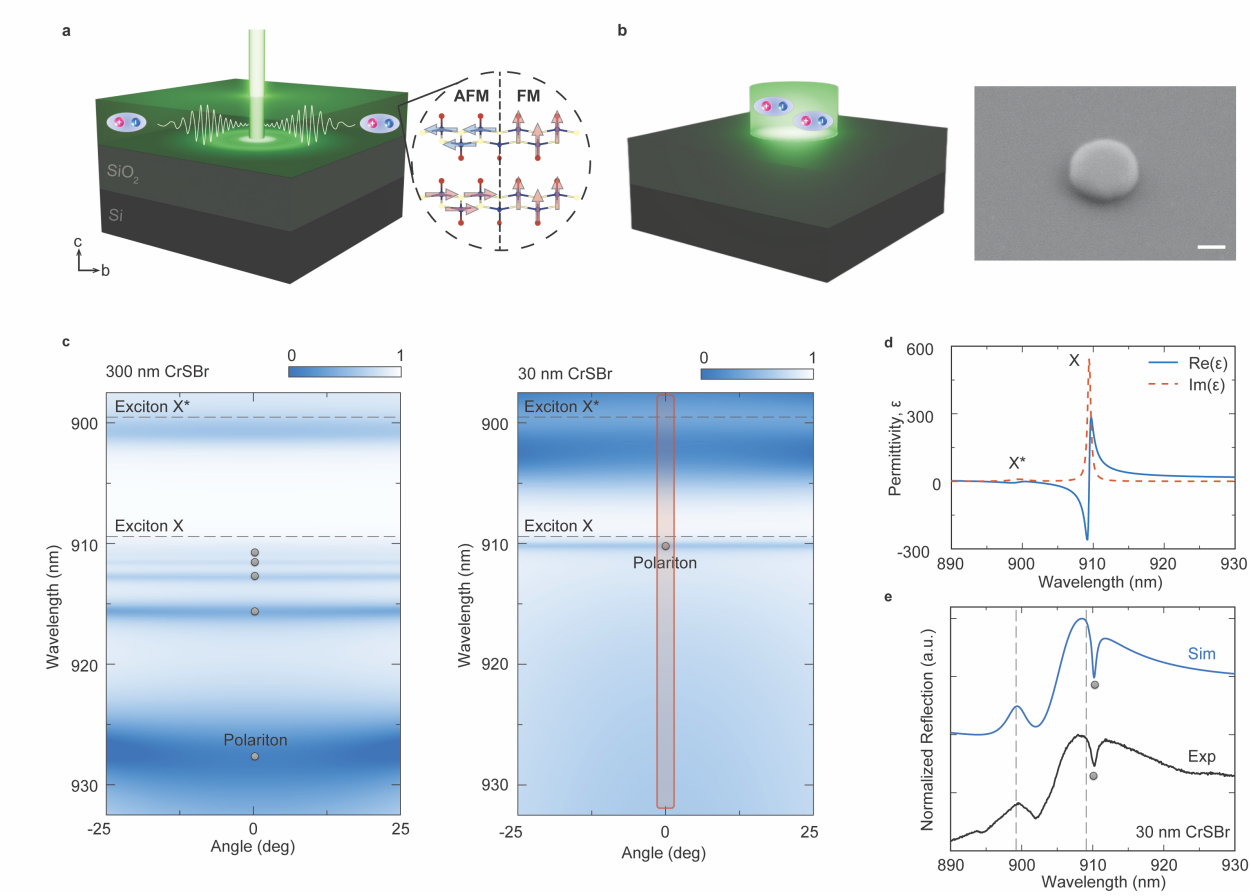

Figure 3.2.1: (a) Schematic of a CrSBr thin film forming a vertical FP cavity because of its high refractive index. The highly confined optical near field strongly interacts with the in-plane excitons in CrSBr and forms exciton-polaritons (EPs) under self-hybridized strong coupling. (b) Left: Schematic of a CrSBr nano-disk patterned by etching a 30 nm thick CrSBr thin film; Right: 45 degrees tilted SEM image of a CrSBr nanodisk of radius 120 nm (scale bar: 100 nm). (c) Simulated angle-resolved reflectance spectra of (left) 300 nm and (right) 30 nm thick CrSBr thin films on a 285nm SiO2/Si substrate, respectively. The dashed lines mark the wavelengths (energies) of two excitons X and X*. Only exciton X is emissive and will be the focus of this study. The grey dots highlight the EP branches arising from the strong coupling between excitons X and cavity photons. (d) The permittivity of CrSBr created by a Lorentz model, which is applied in the simulations. (e) Comparison of simulated and measured reflectance spectra of a 30 nm thick CrSBr thin films on a 285nm-SiO2/Si substrate, under normal-incidence light excitation. The simulated curve is extracted from the orange box in (c).

3.3 Results

CrSBr hosts strongly anisotropic, in-plane excitons whose dipole moments are aligned along the crystallographic b-axis. The high refractive index and layered structure of the material effectively form a natural FP cavity, providing optical feedback without the need for an external resonator. This intrinsic cavity facilitates strong coupling between the confined optical field and the anisotropic excitons, yielding self-hybridized EPs that are predominantly confined within the excitonic dipole plane of the crystal[4,5,23].

To investigate the influence of lateral confinement and to realize EP quantum boxes, we patterned a single exfoliated CrSBr flake into cylindrical microstructures of varying radii (Fig. 1b). This transformation effectively reduces the in-plane dimensionality of the system, spatially confining the in-plane-oriented EP modes. The resulting structures act as lateral potential wells, enabling controlled quantization of the hybrid light-matter states.

To corroborate the existence of the EP states, we simulated the theoretical angle-resolved reflectance spectra of CrSBr thin films in Fig. 1c. The grey dots highlight the EP branches arising from the strong coupling between excitons X and cavity photons. This was done using rigorous coupled-wave analysis (RCWA) through Lorentzian dispersion modeling[4,5,23,28].

$$\varepsilon = \varepsilon_\infty + \sum_j \frac{f_j}{E_{0,j}^2 - E^2 - i\Gamma_j E} \tag{3.1}$$

In this formulation, ε is the complex permittivity, ε_∞ is the background permittivity (11)[4,5,23] $E_{0,j}$ is the excitonic resonance energy, Γ_j is the linewidth, f_j is the oscillator strength. Within our region of interest in the near infrared, CrSBr exhibits two excitons, X and X* with resonances at 4 K of approximately 1.367 eV and 1.377 eV, respectively. This refractive index model allows us to easily turn on and off the excitonic contribution of the CrSBr in simula-

tion to assess the direct role of excitons in our experimental findings.

In thicker CrSBr films, multiple EP branches emerge, as exemplified by the 300 nm film where several modes are clearly resolved (Fig. 1c). To isolate the essential behavior and minimize the influence of multiple interacting branches, we focus on a thinner 30 nm CrSBr film, in which only a single EP branch is observed. This simplification enables a more direct investigation of EP quantum confinement effects.

As a starting point in the fabrication process, bulk CrSBr crystals were mechanically exfoliated onto 285 nm SiO_2/Si substrates, after which a thin film with a confirmed thickness of 30 nm was spin-coated with a poly (methyl methacrylate) resist layer and patterned using electron-beam lithography. The pattern etch mask was realized after a bath in a diluted isopropyl alcohol developer. Inductively coupled plasma (ICP) etching with chlorine-based chemistries selectively removed the unmasked material. Lithography ensured that both etched disks and large thin films originated from a single source flake (Supplementary Fig. 2), enabling direct comparability between disk and thin film observables. The nanodisk devices had radii ranging from 100-255 nm. Each element's height was measured post-fabrication using atomic force microscopy to be consistently 30 nm. The tilted SEM image acquired at 45^o (Fig. 1b) illustrates the well-defined etching profile of the patterned disks.

Although the initial theoretical model to determine the use of the 30 nm thin film was adequate for that analysis, the experimental refractive index was determined by extracting the material permittivity (Fig. 1d) through fitting a Lorentzian dispersion model to the measured thin-film reflectance spectrum at 4 K (Fig. 1e). The resulting model reproduces the experimental reflectance response, revealing an EP branch at 910 nm, and provides the optical parameters used in subsequent simulations. While the EP at 910 nm is the focus of this work, other unidentified optical states[21] are shown in Supplementary Fig. 5.

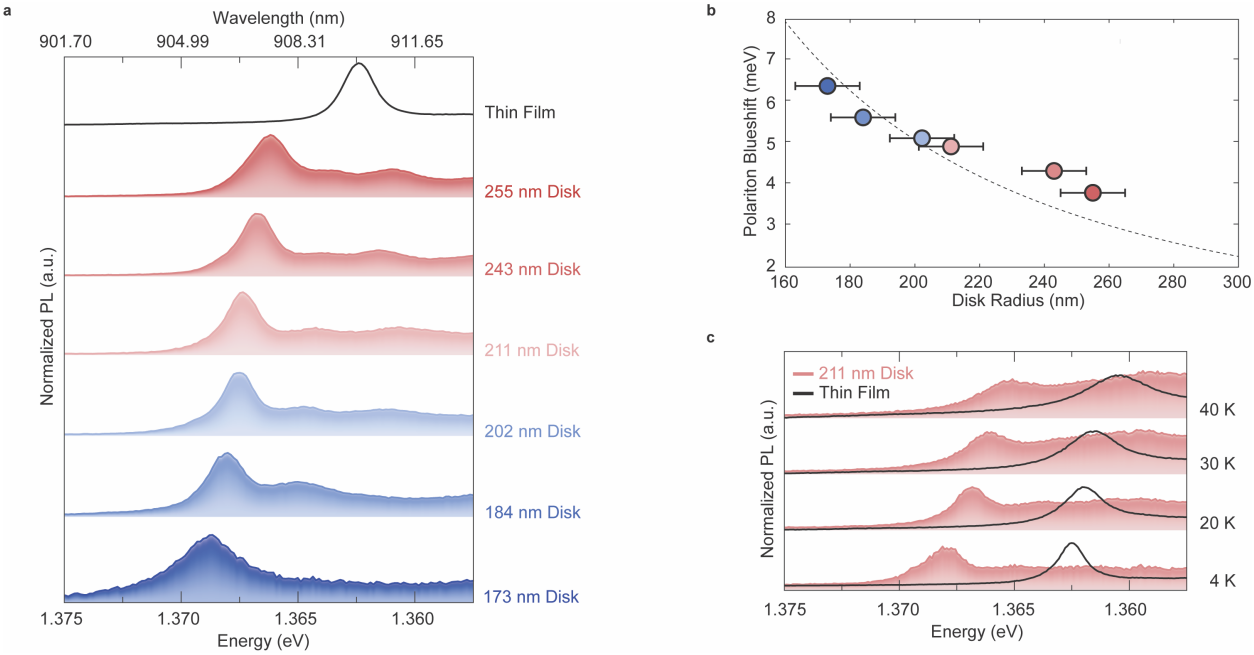

Figure 3.3.1: (a) Photoluminescence (PL) spectra of CrSBr nano-disks of different radii, ranging from 173-255 nm. (b) Polariton PL peak blueshift as a function of CrSBr nano-disk size. The peak values are extracted from (a). The dashed line represents a 1/R2 fit for meff = 0.0011 m0 (c) Temperature-dependent PL spectra of a laterally confined CrSBr quantum box of radius 211 nm compared to the reference Thin Film.

To probe how spatial confinement alters EP properties, we measured the PL spectra of a CrSBr thin film alongside those of individual patterned nanodisks of varying radii (Fig. 2a). The disks' lateral dimensions were determined using atomic force microscopy as shown in Supplementary Fig. 3. As the lateral disk size decreases, the EP resonance systematically blue shifts, revealing the direct influence of confinement on the quantization of the hybrid state energy. This evolution marks the realization of EP quantum boxes: microstructures of CrSBr in which the exciton-photon hybrid becomes confined and energetically discrete.

The total energy shift between the thin film and the narrowest disk (r = 173 nm) approaches 6.4 meV (Fig. 2b). Even larger nanodisks such as when r = 255 nm exhibit a notable blue shift (3.5 meV), considerably more marked energy shift compared to other 2D nanodisk confined systems of similar radii[6].

Figure 2b also includes the expected confinement-induced energy shift for a quasiparticle with

an effective mass of 0.0011 m_0, obtained by fitting the experimental data to a cylindrical quantum confinement model,$\Delta E(R) = \hbar^2\alpha^2/2m_{eff}R^2$, where ΔA is the confinement-induced energy shift, R is the disk radius, and $\alpha = 2.4048$ corresponds to the first zero of the zeroth-order Bessel function.

The extracted effective mass is substantially smaller than the reported mass of bare excitons in CrSBr (0.14 m_0)[30] and is consistent with the hybrid light-matter character of EPs, whose photonic component significantly reduces the quasiparticle mass.

Although the measured energies do not all fall exactly on the fitted curve, they follow the expected $1/R^2$ confinement trend and are in good agreement with the model. The resulting ultralight effective mass and the observed size-dependent energy shifts are therefore consistent with the interpretation of the confined states as EPs.

This pronounced response highlights the exceptional sensitivity of CrSBr's hybrid resonances to geometric confinement, consistent with a substantial photonic contribution that lowers the EP effective mass and extends its de Broglie wavelength.

The enhanced sensitivity of EPs to confinement, relative to purely excitonic systems, establishes structural confinement as an effective and versatile route for tuning light-matter interactions in our layered magnetic semiconductor.

For further confirmation that the observed blueshift arises from an intrinsic shift of the polaritonic state, we performed temperature-dependent PL measurements on a disk with r = 211 nm (r_{211}) and compared them with those of the thin film (Fig. 2c). As the temperature increases, the energy separation between the thin film and r_{211} remains nearly constant, indicating that the confinement-induced shift is intrinsic to the EP state. However, at elevated temperatures, the peak begins to broaden, a feature attributed to its part excitonic composition – another indication of the persistence of the hybridized EP state under confinement.

Along with PL measurements, we performed reflectance measurements, which provide a complementary and simulation-accessible probe of the resonance. Due to the reduced reflectance signal, however, measurements were performed over the disk array regions rather than on individual disks (See AFM images in Fig. 3a). Given the array periodicity of 1.5 µm, which is significantly larger than the resonance wavelength, coupling between neighboring disks is expected to be negligible. To support this claim, we performed a simulation demonstrating the absence of lattice modes when the exciton in CrSBr is turned off: the excitonic contribution to the dielectric response of CrSBr was removed from the simulation, leaving only the background optical response of the material (Fig. 3d).

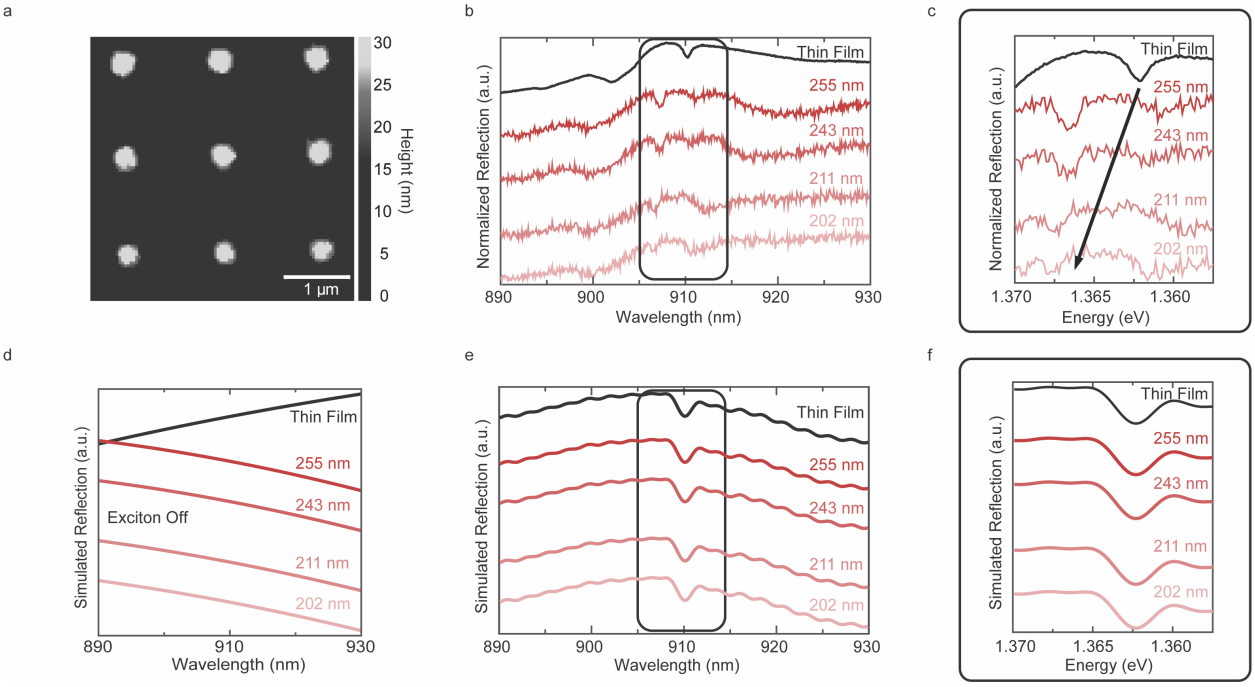

Figure 3.3.2: (a) Atomic force microscopy image of r = 211 nm (b) Differential reflectance spectra of CrSBr nanodisks of different radii, ranging from 202-255 nm (see Methods for details). (c) Magnified view of the spectral region highlighted in (b) shows the blue shift in the EP resonance, similar to the PL spectrum. (d) Reflectance simulation showing the absence of lattice modes when the CrSBr exciton contribution is removed. (e) Full reflectance simulation (electromagnetic) of CrSBr nanodisks including excitonic coupling. (f) Magnified view of the spectral region highlighted in (e). The purely electromagnetic simulation does not capture the blue shift, indicating the origin of the blue shift to be quantum confinement.

The differential reflectance spectrum at 8 K (Fig. 3b and 3c) reveals a clear EP energy

shift, consistent with the trend observed in PL. This agreement supports our interpretation that spatial confinement directly modifies the energy of the self-hybridized EP in CrSBr, and that this confined EP state is the origin of the shifts observed across both reflectance and PL spectra. Unfortunately, the limited signal strength in reflectivity prevented reliable measurements for disks with less than 202 nm radii. The corresponding FDTD electromagnetic reflectance simulations were performed using the permittivity extracted from the reference thin film (Fig. 1e). As shown in Figs. 3e and 3f, the simulated spectra reproduce the experimentally observed spectral features (Fig. 3b and 3c), theoretically confirming the existence of EP in this device geometry. As these simulations capture only the electromagnetic response of the nanodisks (and no quantum confinement), they establish the expected resonance profile of the structures. However, these simulations do not reproduce the experimentally observed systematic blue shift exhibited with increasing lateral confinement. This simulation feature is consistent even under RCWA, where we again observe no resonance shift with disk confinement at the radii of interest (Supplementary Fig. 8). The failure of this classical description to reproduce the size-dependent energy shifts therefore affirms our interpretation that the patterned structures act as EP quantum boxes, and quantum confinement plays an important role in patterned CrSBr nanodisks.

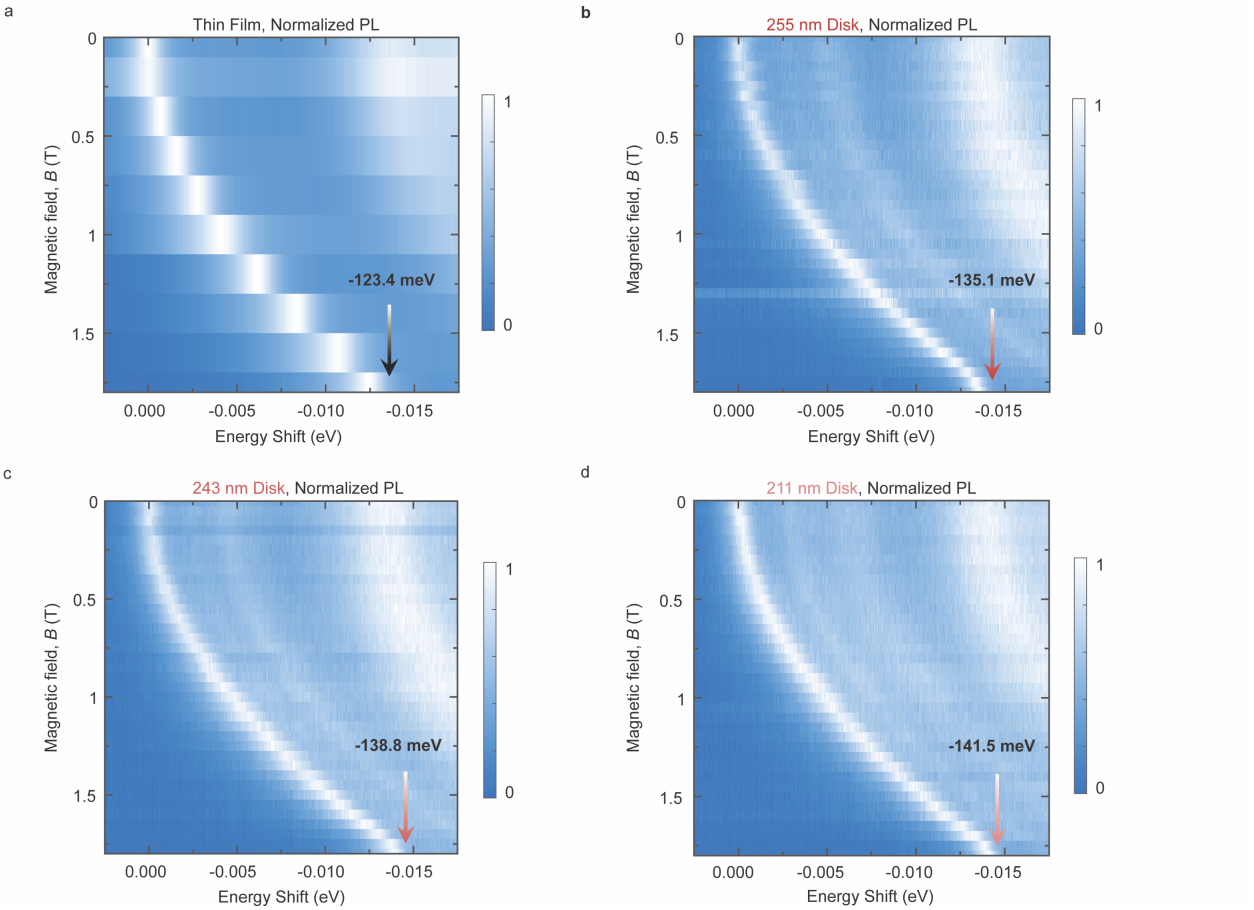

Figure 3.3.3: Magnetic field dependent PL spectra of CrSBr (a) the thin film, a confined disk with radius (b) r = 255 nm (r_{255}), (c) r = 243 nm (r_{243}), and (d) r = 211 nm (r_{211}) showing the evolution of the EP resonance under applied field. All measurements were performed at T = 4 K.

While confinement-induced tuning of the exciton-polariton energy is a matter of considerable remark, its significance could be diminished if coincident with the suppression of the material's intrinsic properties. To assess this, we measured the magnetic-field dependence PL of the thin film and disks r_{211}, r_{243} and r_{255}.

In these magneto-PL measurements, the magnetic field was applied out-of-plane, inducing spin canting rather than a direct transition from AFM to FM order[1]. The thin film CrSBr exhibits AFM and FM ordering at 0 T and approximately 1.8 T, respectively.

Focusing on the EP peak we observe an increase in the magnetic field induced energy shift

with confinement (Fig. 3a). Since the bare thin film is known to support a hybridized EP (Fig. 2a), and prior studies in CrSBr have established that the light-matter ratio of each polariton branch governs its magneto-optical response[4,5] the observation that there is a slightly increased energy shift with greater confinement, implies a slightly more excitonic profile for more confined disks, but with comparable light-matter composition.

The observed energy shift with magnetic field also serves as a confirmation of the persistence of CrSBr's characteristic magneto-optical coupling even under the quantum confinement regime, with consistent confinement signatures in both AFM and FM states. This provides strong evidence that the shifted EP modes have a similar photonic coupling origin to the EP in the thin film but are spectrally displaced due to quantum confinement.

3.4 Discussion

In summary, we demonstrate that geometric engineering in the weak-confinement regime enables systematic tuning of the CrSBr exciton resonance. When combined with the material's intrinsic self-hybridized exciton-polariton states, mesoscopic CrSBr structures exhibit size-dependent quantized EP resonances that preserve the defining properties of the thin film.

The ability to spectrally control an EP resonance not only through spatial confinement but also via magnetic-field tuning underscores the multidimensional tunability of the system. While geometric confinement modifies the photonic environment and quantizes the hybrid mode, the magnetic field directly perturbs the excitonic component through spin-exchange interactions. The coexistence of these two control mechanisms reveals a unique platform in which structural and magnetic degrees of freedom can be used in concert to dynamically engineer EP energies, opening pathways for tailored polaritonic functionalities in integrated and quantum photonic platforms.

3.5 Methods

3.5.1 Fabrication

Using Scotch tape, bulk CrSBr crystals were mechanically exfoliated onto 285 nm SiO_2/Si substrates, after which the flakes were encapsulated with a poly(methyl methacrylate) (PMMA) resist layer using a spin coater. Disk patterns were subsequently defined using a JEOL JBX-6300FS 100 kV electron-beam lithography system, followed by development in a water/isopropanol solution. The desired nanostructures were then realized via chlorine-based inductively coupled
plasma (ICP) etching (Oxford PlasmaLab 100, ICP-1173).

3.5.2 Electromagnetic Simulations

Simulations in Fig. 1c, d and e and Fig. 3d were performed using the Stanford Stratified Structure Solver (S4), a frequency-domain framework for solving Maxwell's equations in layered periodic structures. The solver employs rigorous coupled-wave analysis (RCWA) combined with the S-matrix algorithm and was implemented through a Python interface. Simulations presented in Fig. 3e,f were performed using the finite-difference time-domain (FDTD) solver in Ansys Lumerical.

3.5.3 Optical Measurements

All measurements were carried out in a Montana Instruments cryostat while an attachment of a superconducting solenoidal magnet capable of applying fields up to 7 T in the Faraday geometry was used for field dependent measurements. For PL measurements, a 632.8 nm He-Ne laser was focused to a approximately 1 μm spot at a power of 20 μW using a microscope objective. The emitted signal was spectrally dispersed with a grating spectrometer and detected by a liquid-nitrogen-cooled charge-coupled device (CCD), with a minimum of three frames acquired per measurement. The differential reflectance is defined as (R_sample -

$R_{background})/R_{background}$, where $R_{background}$ is the reflectance of the substrate and R_{sample} is the reflectance of either the CrSBr thin film or the nanodisk. This normalization isolates the optical response of the sample and suppresses contributions from the substrate background.

3.6 Supplementary Information

3.6.1 CrSBr Structure

Supplementary Figure 1 illustrates the crystal structure of CrSBr viewed along three orthogonal crystallographic planes. Chromium sulfide bromide is a layered van der Waals semiconductor. The structure is shown along the a-b, c-a, and c-b crystallographic planes to highlight both the in-plane arrangement of the atoms and the layered stacking along the out-of-plane direction. In the visualization, Cr atoms are represented in blue, S atoms in yellow, and Br atoms in red.

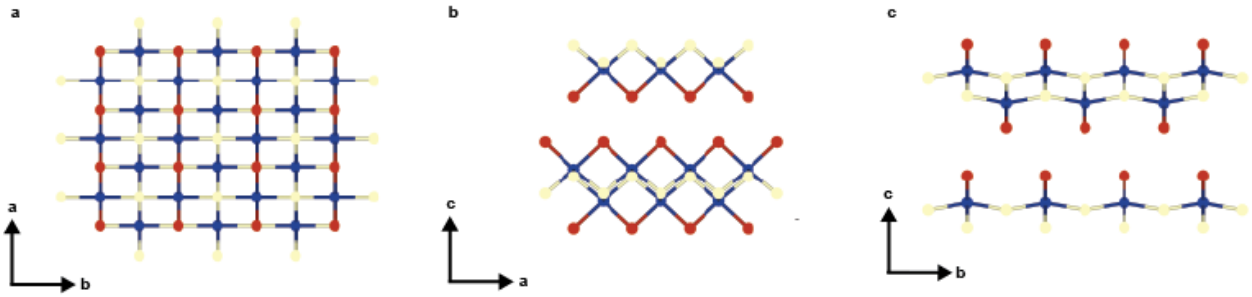

Figure 3.6.1: Crystal structure of CrSBr viewed along the (a) a–b, (b) c–a, and (c) c–b crystallographic planes. The Cr atoms are shown in blue, S in yellow, and Br in red.

3.6.2 Device architecture

Supplementary figure 2 shows an optical microscope image of the device region, highlighting the different measurement areas investigated in this study. Owing to all being the same original source flake the CrSBr thickness was consistently measured to be 30 nm across all three device geometries.

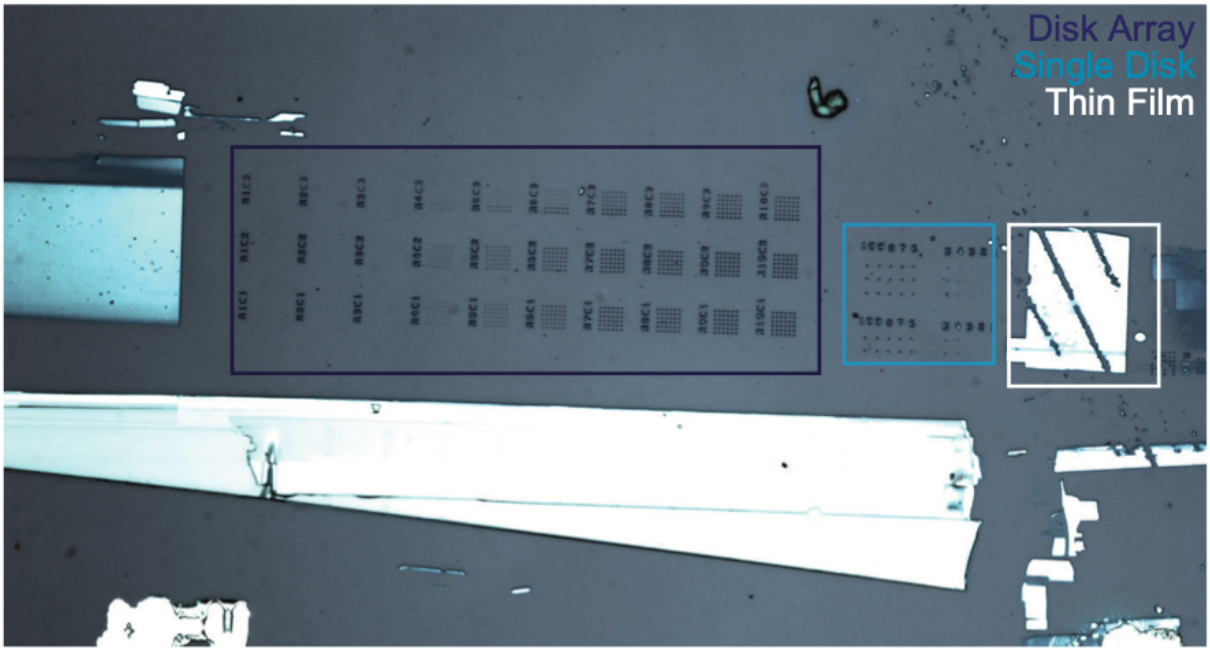

Figure 3.6.2: Device architecture showing the three device regions (i) disk array, (ii) single disk region and (iii) thin film region all from a single flake.

3.6.3 Disk radius

The AFM measured radii likely represent an upper bound on the true disk dimensions due to tip convolution effects. Consequently, the actual disk radii are expected to be slightly smaller than the measured values, which would lead to a correspondingly smaller extracted effective mass. The measurement has an uncertainty of 7 nm from AFM tip convolution effects. An additional uncertainty results from the analysis method with the total uncertainty summing up to 10 nm. The AFM tip design and measurement overestimate the size of the disks meaning the disks are slightly smaller than measurements.

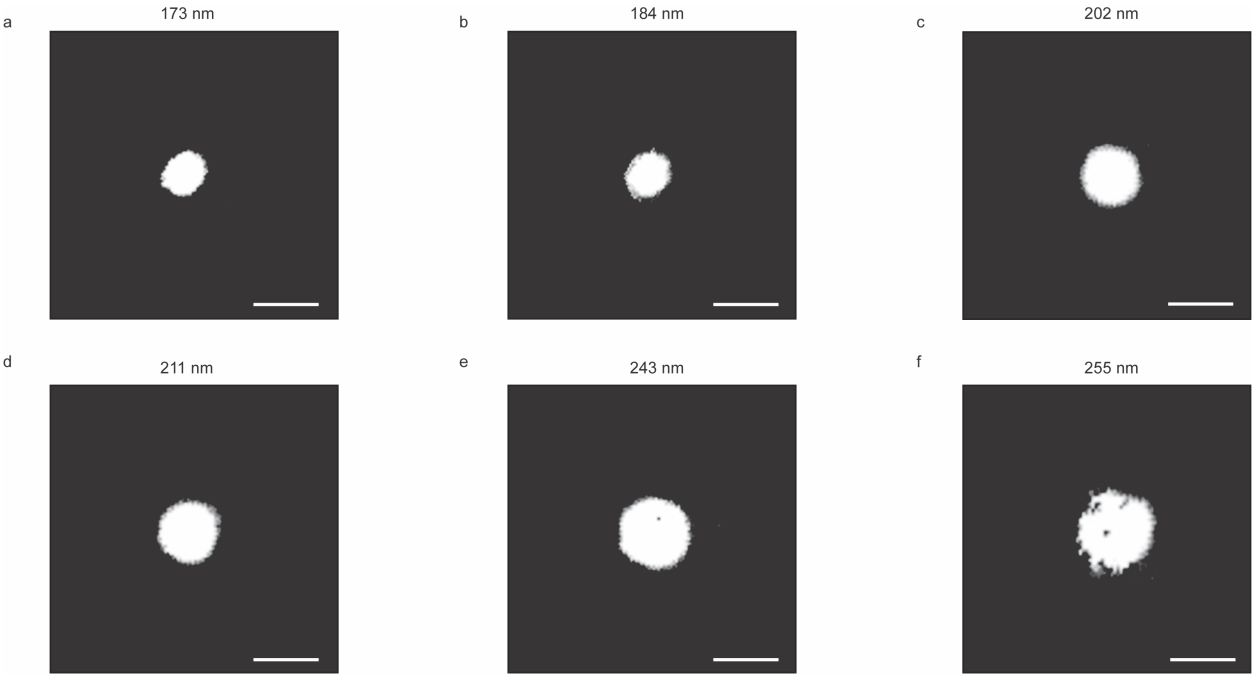

Figure 3.6.3: AFM images of isolated disks with the radii listed above each figure. The measured radii are indicated above each image: (a) r = 173 ± 10 nm, (b) r = 184 ± 10 nm, (c) r = 202 ± 10 nm, (d) r = 211 ± 10 nm, (e) r = 243 ± 10 nm, and (f) r = 255 ± 10 nm. The scale bar in each image corresponds to 500 nm.

3.6.4 Etch quality

Supplementary Figure 3 shows a normal-incidence SEM image of a nominal r = 200nm CrSBr nanodisk. Measurements along two orthogonal in-plane directions yield radii of approximately 202 nm and 192 nm, indicating slight deviations from the designed value. These correspond to dimensional variations of roughly 1–4 %, which are consistent with typical nanofabrication tolerances. Such small deviations likely arise from minor anisotropies in the etching process or edge roughness during pattern transfer. Importantly, these variations remain sufficiently small that they do not qualitatively affect the observed confinement trends or the overall interpretation of the disk behavior.

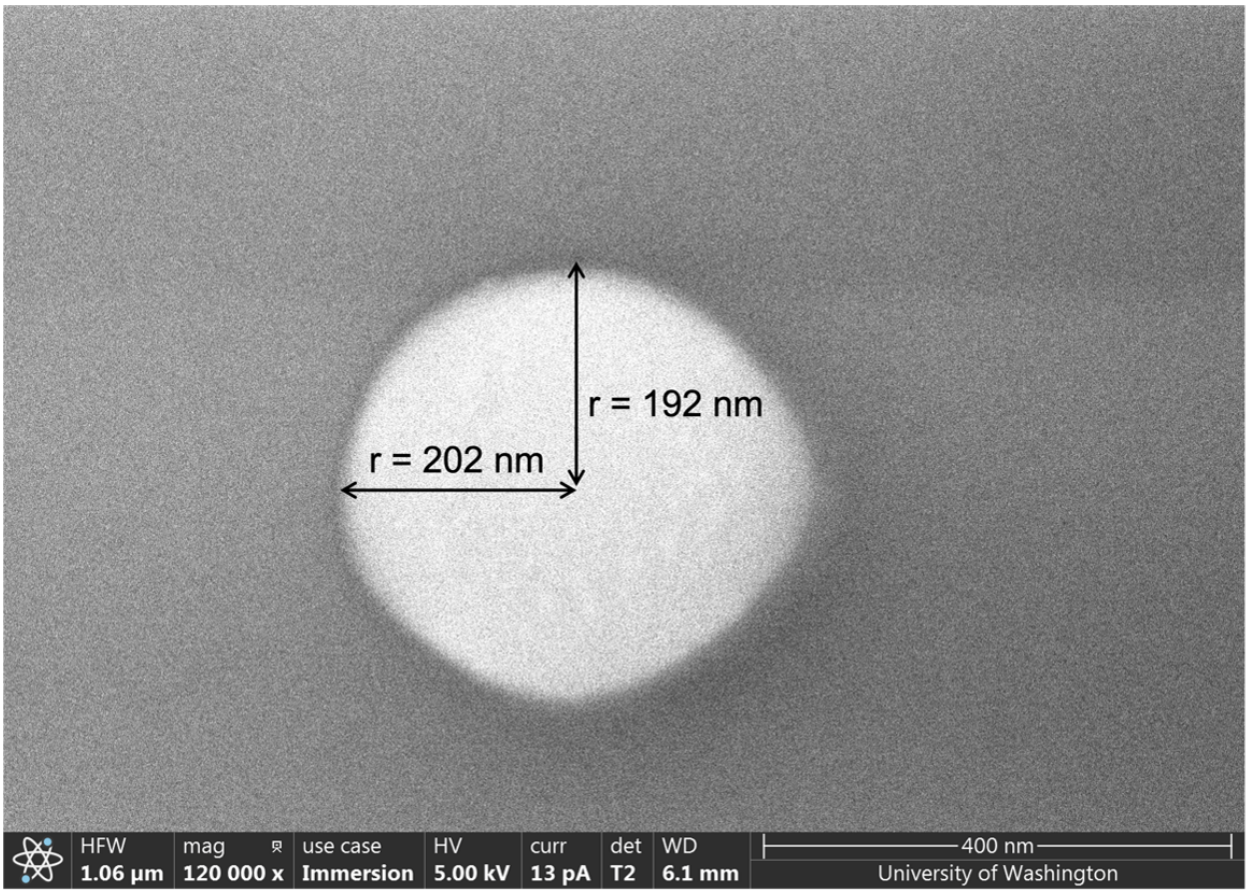

Figure 3.6.4: SEM of r = 200 nm disk. Normal incidence SEM images reveal that deviations of the fabricated disk dimensions from design parameters are approximately 1–4%. These dimensional deviations are within typical nanofabrication tolerances and do not qualitatively affect the observed confinement trends.

3.6.5 PL Spectra of 30 nm CrSBr thin film

Supplementary Figure 4 shows a broader photoluminescence (PL) spectrum of the 30 nm CrSBr thin film, revealing additional spectral features at energies lower than the primary exciton-polariton emission. These weaker peaks have been previously reported in CrSBr and are commonly attributed to defect-related states or otherwise unidentified. While their precise origin remains under investigation, they are not the focus of our analysis, which centers on the EP resonance and its evolution under lateral confinement.

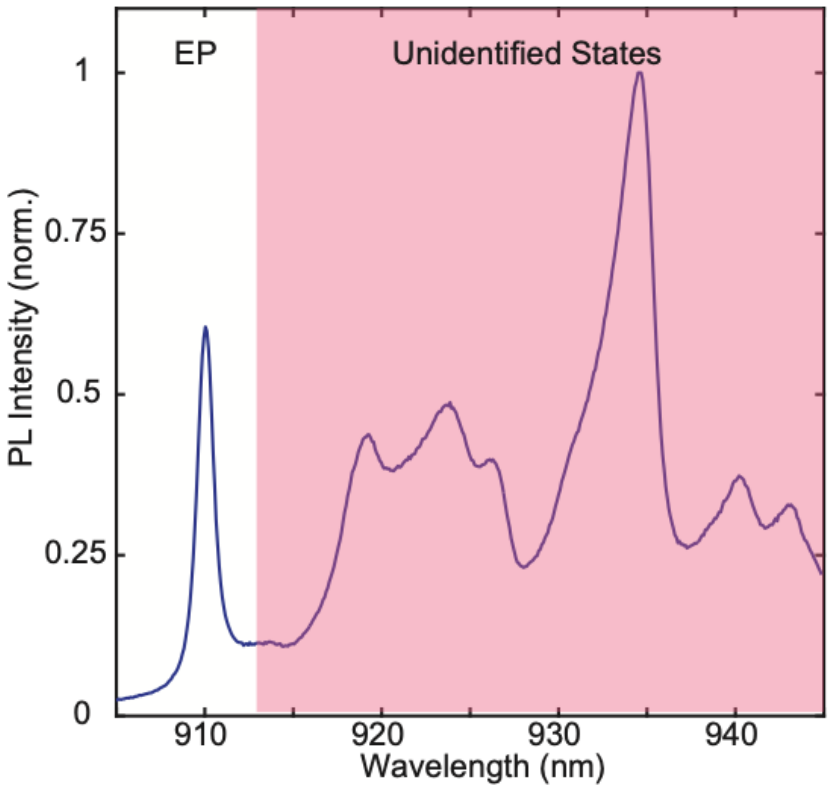

Figure 3.6.5: Broader PL spectra of 30 nm CrSBr Thin Film.

3.6.6 Raman Spectra of 30 nm thin film and r = 211 nm disk

Room-temperature Raman spectra acquired from the parent thin film and the fabricated nanodisks show no discernible changes in the characteristic CrSBr vibrational modes, with peaks observed at 110, 245, and 343 cm^{-1}. Because the Raman excitation spot is larger than the disk diameter, the disk measurement contains a larger relative contribution from the surrounding substrate. Consequently, the feature at 302 cm^{-1}, which is also present in the substrate spectrum, appears more prominently in the disk measurement, although it is detectable in the parent thin film spectrum as well. Both spectra additionally exhibit the Si substrate peak at 518 cm^{-1}.

The consistency of the CrSBr Raman modes of the parent thin film and disks indicates that the fabrication process does not introduce measurable changes does not introduce measurable

changes in stoichiometry or significant strain detectable by Raman within the nanodisks.

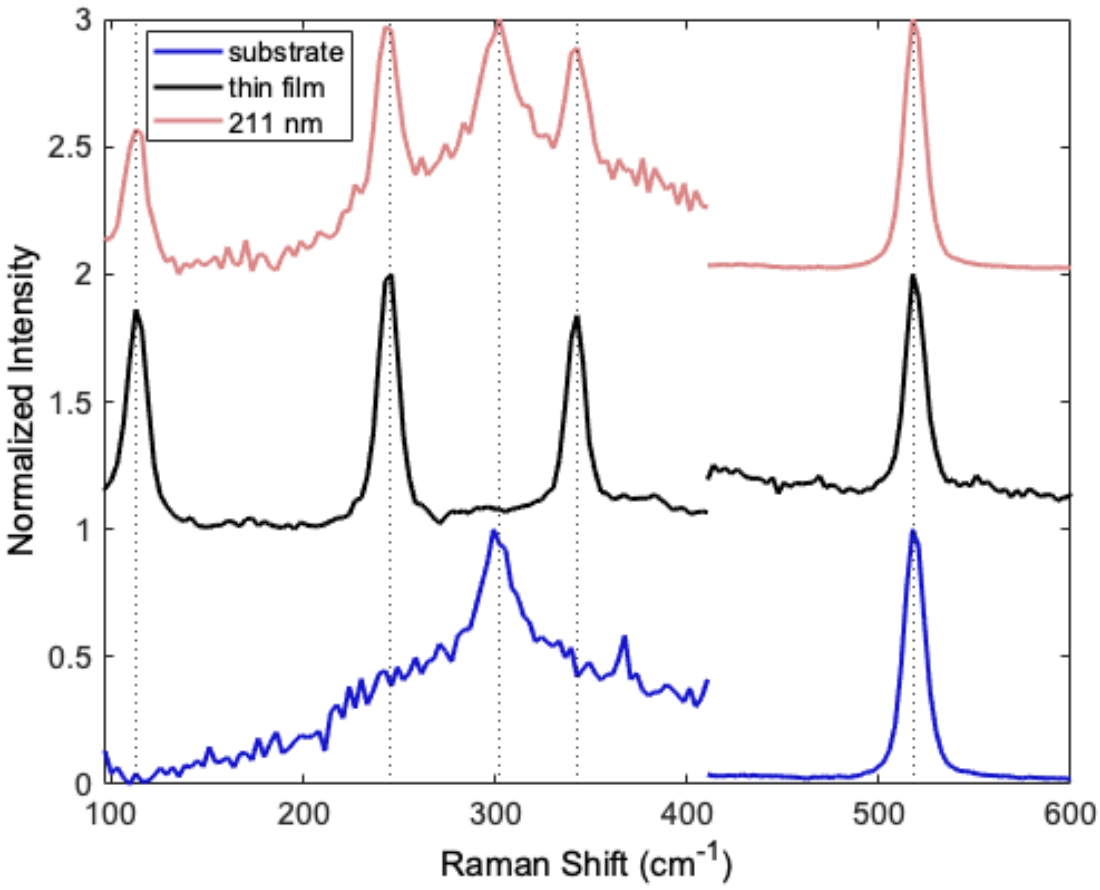

Figure 3.6.6: Room temperature Raman spectra of Si/SiO_2 substrate, 30 nm CrSBr Thin Film, and r = 211 nm nanodisks.

3.6.7 Power dependent PL measurements of r = 211 nm CrSBr disk

To assess the role of laser-induced heating, we measured the power dependence of the r = 211 nm disk. No significant shift in the peak wavelength is observed as the excitation power is increased, indicating that temperature changes arising from optical excitation are not responsible for the observed energy shifts. In addition, the integrated emission intensity scales approximately linearly with excitation power, further supporting the absence of significant thermal effects over the investigated power range.

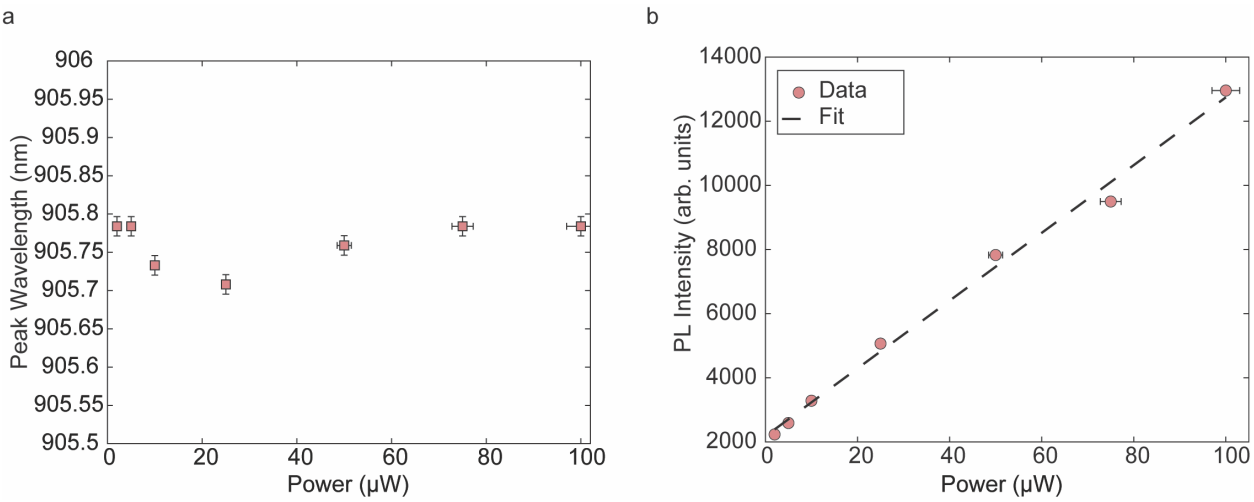

Figure 3.6.7: Peak wavelength versus power of r_{211}. (b) Power dependent intensity of r_{211} with a linear fit.

3.6.8 Linear polarization PL of disks

Supplementary Figure 5 shows the linear polarization-dependent photoluminescence (PL) of the r = 260 nm CrSBr nanodisks. The emission exhibits a clear polarization dependence, consistent with the intrinsic in-plane anisotropy of CrSBr. The EP resonance maintains a strong preferential emission along the crystallographic axis associated with the exciton dipole orientation, indicating that the lateral confinement imposed by the nanodisk geometry does not disrupt the underlying anisotropic optical response of the material.

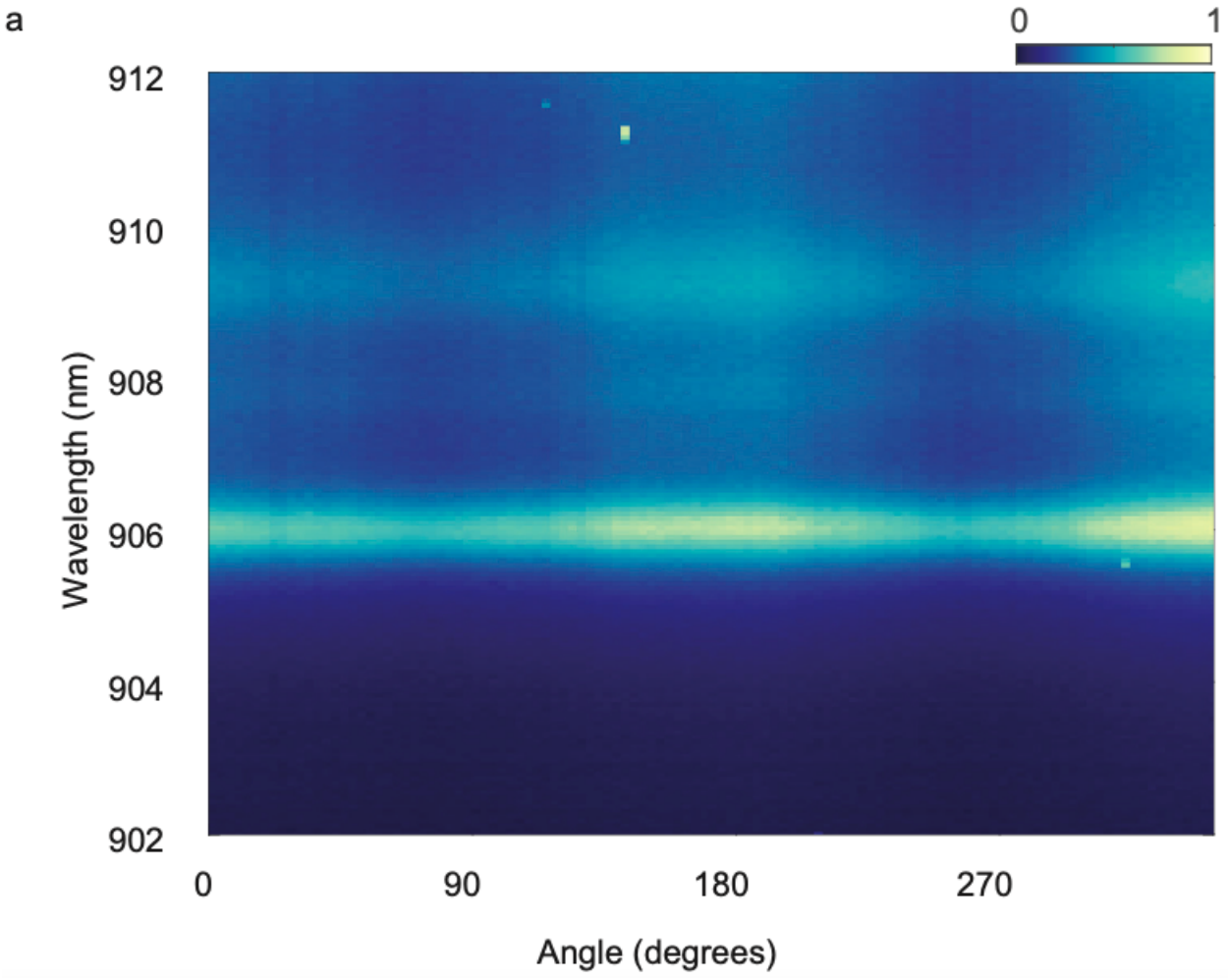

Figure 3.6.8: Linear polarization-dependent PL for r = 260 nm disks highlighting the maintained EP anisotropy.

3.6.9 RCWA Simulated reflectance spectra of disks

While FDTD simulations accurately capture the electromagnetic response of the nanodisk structures, we additionally performed RCWA calculations and found no evidence of confinement induced polariton energy shifts. This result remained consistent across a range of periodic boundary conditions exceeding the disk separation distance. Although both approaches reproduce the overall spectral characteristics of the devices, neither predicts the systematic blue shift observed experimentally with increasing lateral confinement. The inability of these classical electromagnetic models to account for the size-dependent energy

evolution provides further evidence that the observed shifts do not originate from purely photonic effects. Instead, the discrepancy supports our interpretation that the confinement-induced spectral evolution arises from the quantum nature of the EP states.

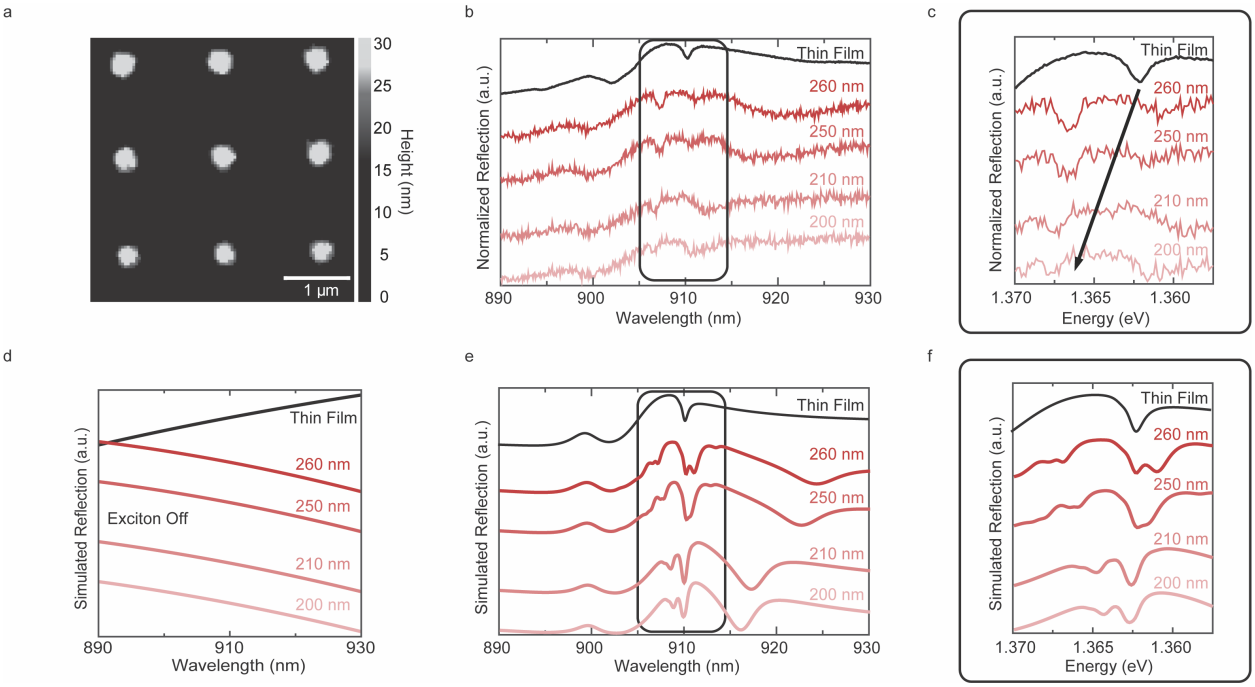

Figure 3.6.9: (a) Atomic force microscopy image of r = 210 nm (b) Differential reflectance spectra of CrSBr nanodisks of different radii, ranging from 200-260 nm. (c) Magnified view of the spectral region highlighted in (b) shows the blue shift in the EP resonance, similar to the PL spectrum. (d) Reflectance simulation showing the absence of lattice modes when the CrSBr exciton contribution is removed. (e) Full reflectance simulation (electromagnetic) of CrSBr nanodisks including excitonic coupling. (f) Magnified view of the spectral region highlighted in (e). The purely electromagnetic simulation does not capture the blue shift, indicating the origin of the blue shift to be quantum confinement.

3.6.10 Confinement effects on 50 nm and 105 nm CrSBr nanodisks

Additionally, as CrSBr layers become thicker but remain within the mesoscopic range, the photonic contribution to the in-plane EPs increases. This can be observed in the increasingly dispersive branches emergent in larger thin films of the material[4], which results in a lower effective mass for the particles and an accompanied longer de Broglie wavelength. Investigating confinement in thicker CrSBr disks could offer support for the view that the

exceptional confinement sensitivity arises from the ultralow effective mass of the EPs, which amplifies their response to in-plane nanoscale potential modulation.

Although a direct thin-film reference from the same source was unavailable, the quantization behavior is also evident in nanodisks fabricated from a 50 nm and 105 nm thick CrSBr film. In these cases, increasing lateral confinement similarly produced a blue shift in the EP energy.

A comparison between these thicker disks reveals that increasing the thin-film thickness enhances the sensitivity of the EP to lateral confinement (Supplementary Fig. 6). This trend reinforces our hypothesis that the stronger photonic contribution in CrSBr EPs extends the de Boglie wavelength, thereby amplifying the sensitivity of the EP to spatial confinement. In essence, the thicker disks host EPs that behave more like photons and thus are more responsive to nanoscale potential modulation. It is worth noting that for the 105 nm disks multiple branches are present but only the lowest energy branch – the most polaritonic – is tracked.

a

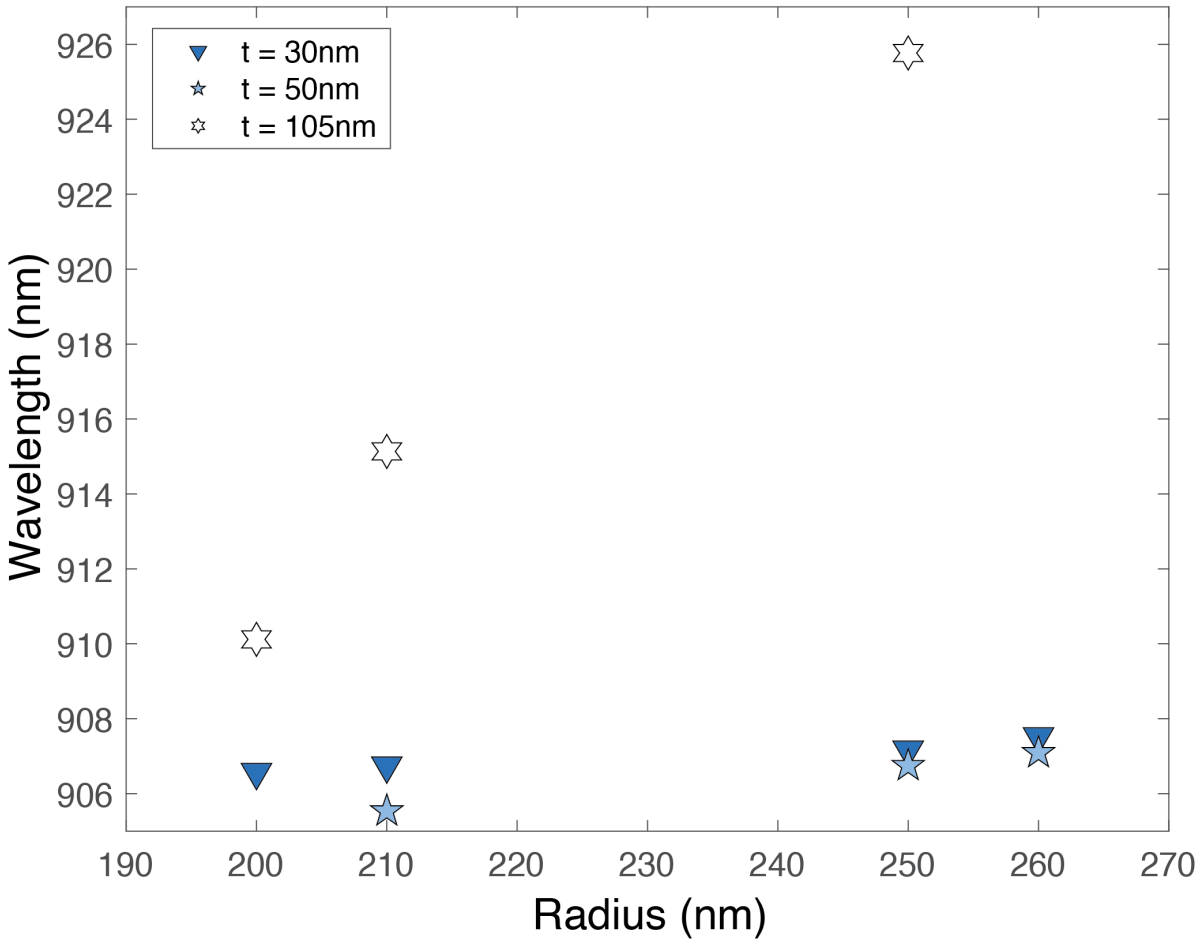

Figure 3.6.10: (a) PL spectra data of disks of varying thicknesses providing additional data points for the shift of the EP energy with confinement: confirming the consistency of the geometry dependent effect across devices

3.7 Bibliography

1. Kuznetsov, A. S. et al. Quantum confinement of exciton-polaritons in a structured (Al,Ga)As microcavity, Phys. Rev. B 97, 195309 (2018).

2. El Daïf O. et al. Polariton quantum boxes in semiconductor microcavities, Appl. Phys. Lett 88, 061105 (2006).

3. Wilson, N.P., Lee, K., Cenker, J. et al. Interlayer electronic coupling on demand in a 2D magnetic semiconductor. Nat. Mater. 20, 1657–1662 (2021).

4. Dirnberger, F., Quan, J., Bushati, R. et al. Magneto-optics in a van der Waals magnet tuned by self-hybridized polaritons. Nature 620, 533–537 (2023).

5. Wang, T., Zhang, D., Yang, S. et al. Magnetically-dressed CrSBr exciton-polaritons in ultrastrong coupling regime. Nat Commun 14, 5966 (2023).

6. Wei, G., Czaplewski, D.A., Lenferink, E.J. et al. Size-tunable Lateral Confinement in Monolayer Semiconductors. Sci Rep 7, 3324 (2017).

7. Semina, M. A. et al. Excitons and Trions in CrSBr, Phys. Rev. B 111, 205301 (2025)

8. Han, B., et al. Exciton-polariton condensate in the van der Waals magnet CrSBr, arXiv:2431.18233 [cond-mat.mtrl-sci], (2025)

9. Trauzettel, B., Bulaev, D. V., Loss, D. Burkard, G. Spin qubits in graphene quantum dots. Nature Phys. 3, 192–196 (2007).

10. Loss, D. DiVincenzo, D. P. Quantum computation with quantum dots. Phys. Rev. A 57, 120 (1998).

11. Petta, J. R. et al. Coherent manipulation of coupled electron spins in semiconductor quantum dots. Science 309, 2180–2184 (2005).

12. Kang, J. et al. Thickness sorting of two-dimensional transition metal dichalcogenides via copolymer-assisted density gradient ultracentrifugation. Nature Commun. 5 (2014).

13. Gan, Z. X. et al. Quantum confinement effects across two-dimensional planes in MoS2 quantum dots. Appl. Phys. Lett. 106, 233113 (2015).

14. Gopalakrishnan, D. et al. Electrochemical synthesis of luminescent MoS2 quantum dots. Chem. Commun. 51, 6293–6296 (2015).

15. Jin, H. et al. Colloidal single-layer quantum dots with lateral confinement effects on 2D exciton. J. Am. Chem. Soc. 138, 13253–13259 (2016).

16. Lee, J. et al. Uniform graphene quantum dots patterned from self-assembled silica nanodots. Nano Letters 12, 6078–6083 (2012).

17. Woggon, U. Optical Properties of Semiconductor Quantum Dots (Springer, 1997)

18. Seyler, K. L. et al. Ligand-field helical luminescence in a 2D ferromagnetic insulator. Nat. Phys. 14, 277–281 (2018).

19. Zhang, Z. et al. Direct photoluminescence probing of ferromagnetism in monolayer two-dimensional CrBr3. Nano Lett. 19, 3138–3142 (2019).

20. Kang, S. et al. Coherent many-body exciton in van der Waals antiferromagnet NiPS3. Nature583, 785–789 (2020).

21. Klein, J. et al. The bulk van der Waals layered magnet CrSBr is a quasi-1D quantum material. ACS Nano 17, 5316–5328 (2023).

22. Canales, A., Baranov, D. G., Antosiewicz, T. J. Shegai, T. Abundance of cavity-free polaritonic states in resonant materials and nanostructures. J. Chem. Phys. 154, 024701 (2021).

23. Demir, A.K., Nessi, L., Vaidya, S. et al. Tunable nanophotonic devices and cavities based on a two-dimensional magnet. Nat. Photon. (2025). https://doi.org/10.1038/s41566-025-01712-2

24. Göser, O., Paul, W. & Kahle, H. G. Magnetic properties of CrSBr. J. Magn. Magn. Mater. 92, 129–136 (1990)

25. Bae, Y. J. et al. Exciton-coupled coherent magnons in a 2D semiconductor. Nature 609, 282–286 (2022)

26. Diederich, G. M. et al. Tunable interaction between excitons and hybridized magnons in a layered semiconductor. Nat. Nanotechnol. 18, 23–28 (2023)

27. Ruta, F.L., Zhang, S., Shao, Y. et al. Hyperbolic exciton polaritons in a van der Waals magnet. Nat Commun 14, 8261 (2023).

28. Fang, J., Kala, A., Johnson, R. et al. Free space few-photon nonlinearity in critically coupled polaritonic metasurfaces. Nat Commun 16, 10099 (2025).

29. Weber, T. et al. Intrinsic strong light–matter coupling with self-hybridized bound states in the continuum in van der Waals metasurfaces. Nat. Mater. 22, 970–976 (2023)

30. Liebich, M. et al., Controlling Coulomb correlations and fine structure of quasi-one-dimensional excitons by magnetic order. Nat. Mater. 24, 384–390 (2025).

Chapter 4

In Situ Strain Tuning of 2D Material-Integrated Nanocavity

This chapter contains contents from a published manuscript in which I was a co-author. My contribution to the work was the material determination and device transfer. The text has been adapted for inclusion in this dissertation: A. Manna, J. E. Fröch, J. Cenker, **S. Pumulo**, A. W. Barnard, J.H. Chu, X. Xu, and A. Majumdar, "Cryo-Compatible In Situ Strain Tuning of 2D Material-Integrated Nanocavity," ACS Photonics, vol. 10, no. 9, pp. 3242–3247, Sep. 2023.

4.1 Background

While the field of material-integrated photonics has shown tremendous promise[1–4,4–11], the inability to tune cavity resonances after fabrication remains a significant challenge. This work addresses the issue of achieving resonance matching between integrated photonic cavities and low-dimensional materials. A mechanic-strain tunable GaP nanobeam cavity was fabricated to accomplish this adapting previous methods[43–47]. Once fabricated it was coupled to a monolayer WSe_2 flake. This approach enabled continuous tuning of the cavity resonance over a range of approximately 5 nm while maintaining the cavity quality factor. These results

demonstrate the potential of strain as an on-device tuning mechanism for overcoming post-fabrication detuning, enabling more reliable resonance matching and stronger light-matter coupling in material-integrated photonic devices.

4.2 Fabrication and Design

4.2.1 Cavity Design

The cavity design was based on a one-dimensional (1D) nanobeam cavity, where the resonant mode is determined by the geometry of the periodic hole array, which defines the effective refractive index and photonic band structure of the cavity. GaP was selected as the dielectric material owing to its high refractive index ($n \approx 3.2$) in the visible spectral range. Combined with the low refractive index of the supporting polyimide substrate ($n \approx 1.5$), this provides a large refractive index contrast, enabling strong optical confinement and the realization of high-quality-factor cavities by minimizing radiative losses into the substrate.

The cavity geometry was designed using established optimization procedures described previously[54]. The photonic band structure was first calculated using the MIT Photonic Bands (MPB) software package[55], after which the cavity geometry was optimized using the Ansys Lumerical finite-difference time-domain (FDTD) electromagnetic solver to maximize the cavity quality factor.

The nanobeam cavity consists of a 215 nm thick, 393 nm wide GaP membrane supported on a silicon substrate. Optical confinement is achieved using a defect region comprising ten elliptically shaped air holes whose dimensions are quadratically tapered, while the cavity mirrors consist of fifteen Bragg reflector holes on either side of the defect. Throughout the structure, the minor axis radius of the elliptical holes is fixed at 51 nm. Within the taper region, the major axis radius is varied from 81 nm at the cavity mirrors to 123 nm at the cavity center, while maintaining a constant center-to-center hole spacing of 160 nm. The

Bragg mirror sections retain a major axis radius of 81 nm with the same periodicity. Using these optimized design parameters, simulations predicted a fundamental cavity resonance at 792.4 nm with a $Q = 2.56 \times 10^6$.

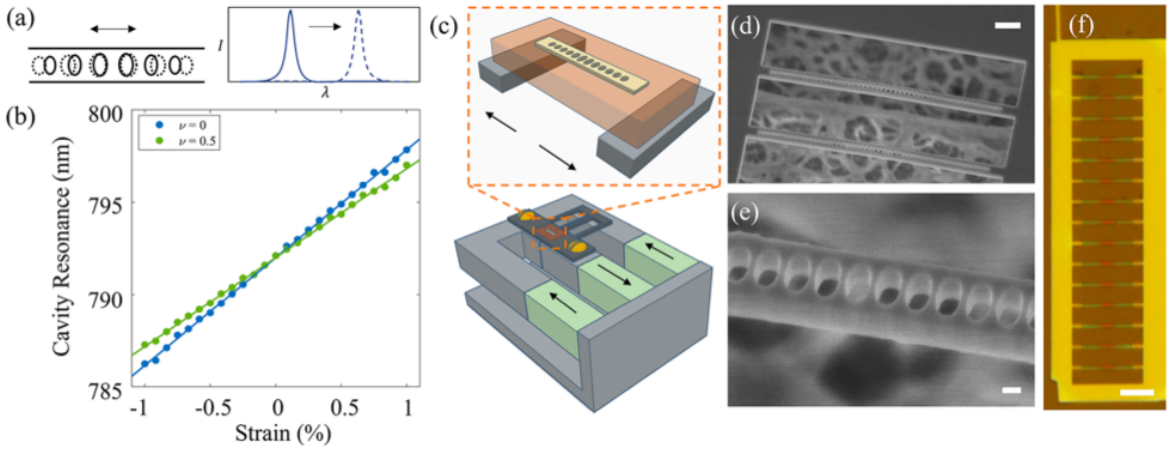

Figure 4.2.1: (a) Schematic demonstrating how longitudinal strain translates to a shift in the cavity resonance of a 1D PCC. (b) Extracted variation of the cavity resonance wavelength with longitudinal uniaxial strain at extremes of the Poisson ratio ν from 3D FDTD simulations. (c) Schematic of a nanobeam transferred on top of a polyimide substrate (top panel), which is glued to a titanium backing and flexure (bottom panel). Three piezo stacks (green) are configured in parallel, which are actuated in opposite directions as indicated by the black arrows. SEM images of floating nanobeams, prior to transfer: (d) an overview of the nanobeams with the surrounding GaP frame (scale bar: 1 μm). The porous, rough structures are on the etched Si surface underneath the released GaP nanobeams. (e) High-resolution zoomed-in view of the cavity region of a nanobeam (scale bar: 100 nm). (f) Optical image of a 1D PCC array transferred onto the polyimide substrate (scale bar: 5 μm). Reproduced with permission from Ref. 1 Copyright © 2023 American Chemical Society.

The nanobeam cavity was fabricated on a polyimide substrate that was epoxied onto a strain cell actuated by three piezoelectric stacks arranged in a parallel configuration. Mechanical strain was transferred from the piezoelectric actuators to the polyimide substrate through controlled expansion and contraction of the piezo stacks. The outer and inner piezoelectric elements are oppositely poled such that the outer actuators expand under an applied positive voltage, while a negative voltage produces the opposite response. As the polyimide substrate deforms, the applied strain is uniformly transferred to the nanobeam cavity.

The applied strain modifies the cavity resonance through changes in both the cavity geometry and the optical properties of the dielectric material. Mechanical deformation alters the lattice periodicity and physical dimensions of the nanobeam, these effects shift the resonant wavelength, providing continuous and reversible tuning of the cavity resonance.

A 20 μm-thick polyimide substrate was used and bonded to the two-dimensional flexure sample plates (Razorbill Instruments) using epoxy (Stycast 2850 FT). An additional advantage of the three-piezo actuator design, compared with directly mounting the sample onto a single piezoelectric stack, is the substantial reduction of thermally induced strain during cooling, ensuring reliable operation under cryogenic conditions. This is because the large thermal expansion of the outer two piezo stacks gets compensated by the expansion of the middle piezostack, ensuring the transferred device on the polyimide does not break going through the cooldown process in the cryostat.

4.2.2 Device Fabrication

The fabrication process consists of two stages: nanobeam cavity fabrication followed by material integration. The cavity fabrication begins with spin coating a layer of ZEP 520A electron beam resist onto the 215 nm GaP substrate. The nanobeam pattern is then defined using electron beam lithography (EBL), after which the pattern is transferred into the GaP layer by reactive ion etching using an $Ar/Cl/N_2$ plasma. Finally, an isotropic XeF_2 etch is performed to selectively remove the underlying sacrificial layer, releasing the GaP nanobeam cavity and leaving it suspended.

Following cavity fabrication, the material integration process described in Section 2.3.2 is employed. Bulk WSe_2 crystals are mechanically exfoliated using adhesive tape until sufficiently thin flakes are obtained. The exfoliated material is then transferred onto a plasma-cleaned 285 nm SiO_2/Si substrate and inspected under an optical microscope to identify a suitable monolayer flake.

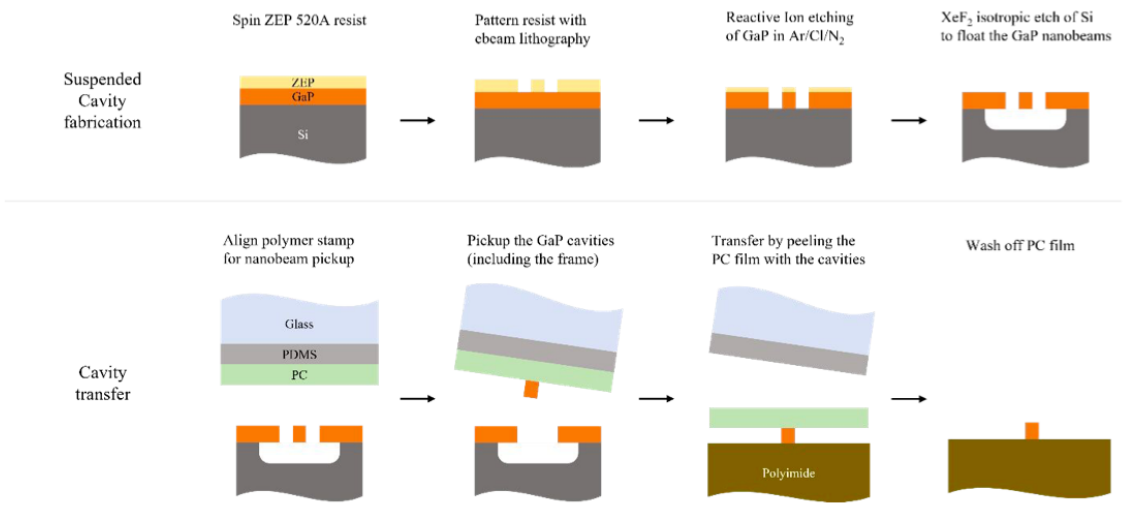

Figure 4.2.2: Figure demonstration of device fabrication process. Reproduced with permission from Ref. 1 Copyright © 2023 American Chemical Society.

A dry transfer process is subsequently used to assemble the device. A PC/PDMS polymer stamp, mounted on a temperature-controlled transfer stage, is first used to pick up the suspended nanobeam cavity before transferring it onto the polyimide strain substrate. The selected monolayer WSe_2 flake is then transferred using the same dry transfer technique and precisely aligned onto the nanobeam cavity. The resulting integrated WSe_2-nanobeam device forms the final structure investigated.

4.3 Results

The first step in the analysis of the devices is looking at the pre-material integration characterization of the devices to understand the behavior of the nanobeam cavities. The figure

shows that under 532 nm excitation using continuous wave (CW) laser. We observed a 3 nm red shift in the cavity resonance peak, which is slightly larger than the expected 1.8 nm shift from the FDTD simulation. We attribute this difference to a remnant strain from the dry transfer process, which was used to place the PCCs on the polyimide substrate. We further note a small reduction of around 10 percent in the Q-factor after transfer, which is expected due to the change in the background refractive index.

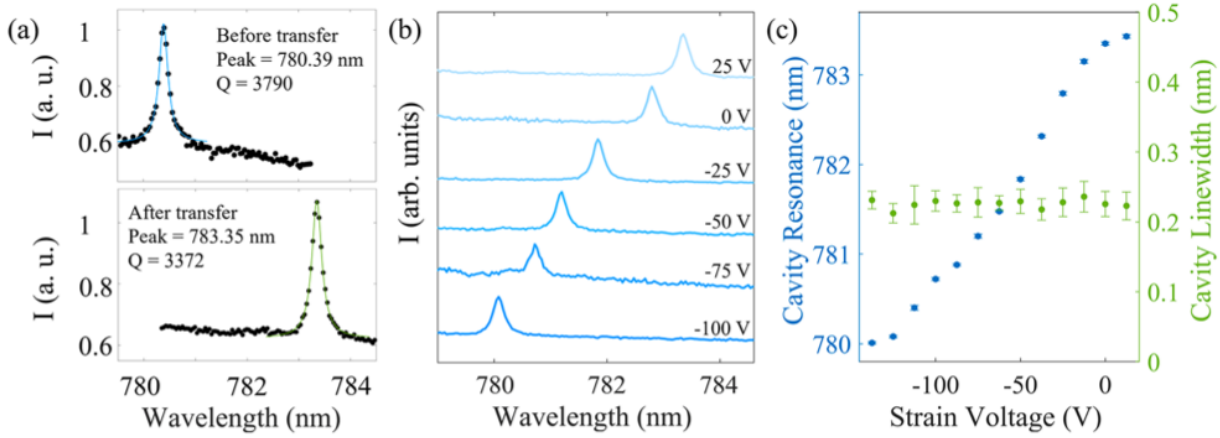

Figure 4.3.1: Device characterization at room temperature. (a) Comparison of the PL spectrum (from intrinsic GaP background) before and after transfer is shown in the top and bottom panels, respectively. Resonance peaks and quality factors were extracted, using a Lorentzian fit on the data. (b) Waterfall plot of the nanobeam spectrum at selected piezo voltages. (c) Cavity resonance wavelengths and line widths as a function of applied piezo voltage. Reproduced with permission from Ref. 1 Copyright © 2023 American Chemical Society.

The strain-tuning capability of the cavity-on-strain-cell device was first characterized at room temperature by applying a voltage across the piezoelectric actuators, thereby inducing strain in both the polyimide substrate and the suspended cavity. As the applied voltage was varied, a clear and continuous shift in the cavity resonance was observed (Fig. 2.3(b)). Tracking the cavity resonance as a function of the applied piezo voltage revealed a saturation in the tuning response beyond the voltage range of approximately -130 to 10 V (Fig. 2.3(c)). These voltages correspond to the maximum compressive and tensile strains that could be applied before the nanobeam began to slip on the polyimide surface, limiting the room-temperature

tuning range of the cavity resonance to approximately 3.5 nm. The asymmetric voltage range arises from remnant strain introduced during the dry transfer process.

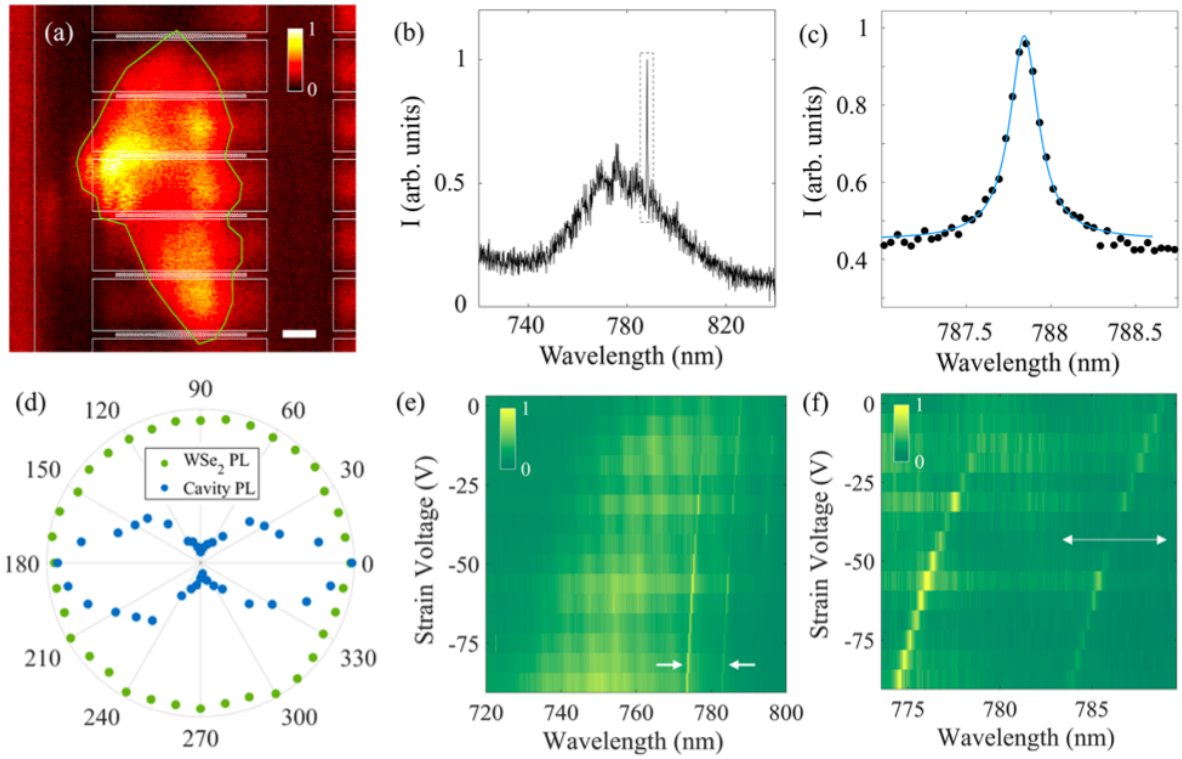

Figure 4.3.2: PL of monolayer WSe2 integrated with the GaP PCC array. (a) Scanning PL map of the monolayer WSe2-integrated nanobeam cavities on polyimide. The WSe2 region is outlined in green, while the nanobeam cavities (with the supporting GaP frame) are outlined in white. The scale bar is 2 μm. (b) PL spectrum measured from the center of a nanobeam (at a piezo voltage of -25 V) showing the cavity-enhanced PL over the broad monolayer exciton resonance. (c) A zoomed-in view of the cavity PL spectrum fit with a Lorentzian function. (d) Polarization polar diagram of the PL intensity, extracted from spectra. (e) 2D map of the normalized cavity spectrum with the applied strain voltage and wavelength. The two cavity modes are indicated by the white arrows. (f) Zoomed-in view of the strain-tunable cavity modes, with the white double arrow indicating the mode tuning range. Reproduced with permission from Ref. 1 Copyright © 2023 American Chemical Society.

We next demonstrate the integration of the cavity with a vdW material while retaining strain tunability under cryogenic conditions. A monolayer WSe_2 flake was mechanically isolated and dry-transferred onto a set of cavity-on-strain-cell devices with designed cavity resonances near the WSe_2 exciton transition ($\sim$ 775 nm). The integrated device was characterized

using PL spectroscopy at 5 K under excitation from a continuous-wave 532 nm laser, with a scanning mirror used to obtain spatial PL maps. The resulting PL map is shown in Fig. 2.4(a). Variations in the PL intensity across the monolayer primarily originate from structural inhomogeneities introduced during the dry transfer process.

Spectral measurements reveal a pronounced enhancement of the PL at the cavity resonance, as shown in Fig. 2.4(b). The cavity-coupled emission exhibits a linewidth of 0.23 nm (Fig. 2.4(c)), comparable to that measured from bare GaP cavities fabricated on polyimide, indicating that the material transfer process introduces minimal degradation to the optical quality of the cavity. From the measured spectra, a PL enhancement factor of approximately two is extracted. Although this enhancement appears modest, the excitation and collection spot size in the optical setup is significantly larger than the spatial extent of the cavity mode. Consequently, the measured signal contains a substantial contribution from uncoupled WSe_2 emission, implying that the local enhancement within the cavity mode volume is considerably larger than the measured value.

The coupling between WSe_2 and the PCC was further confirmed through polarization-resolved PL measurements. Figure 2.4(d) compares the linearly polarized cavity-coupled emission with the background WSe_2 PL. Unlike the nearly polarization-independent emission from the monolayer, the cavity-coupled PL exhibits a pronounced polarization dependence that reflects the strongly polarized nature of the nanobeam cavity mode. The polar plot shows that the enhanced emission is aligned with the expected polarization axis of the PCC, where 0° is referenced to the polarization orientation of the optical measurement system.

Applying strain to the integrated device results in continuous tuning of the cavity resonance, as shown by the normalized cavity-coupled PL spectra in Fig. 2.4(e). Two cavity modes are observed, both exhibiting resonance shifts of approximately 5.5 nm (Fig. 2.4(f)), corresponding to more than an order of magnitude larger than the cavity linewidth. Throughout the tuning range, the cavity linewidth remains nearly constant, demonstrating that the applied

strain does not significantly degrade the cavity quality. In contrast, the background PL from the monolayer WSe_2 undergoes a substantially larger redshift than the cavity resonance. This behavior is attributed to more efficient strain transfer into regions of the monolayer that are in direct contact with the polyimide substrate, whereas the suspended portion above the cavity experiences a different strain distribution. Furthermore, strain intrinsically redshifts the excitonic transitions of monolayer WSe_2,[49] and the spatially varying strain profile created as the monolayer drapes over the nanobeam gives rise to an effectively broadened PL emission.

4.4 Conclusion

In this work, we demonstrated reversible strain tuning of a PCC over a wavelength range of approximately 5 nm, enabling enhanced light-matter coupling while maintaining minimal degradation of the cavity quality. Furthermore, we showed that this tuning mechanism remains effective under cryogenic conditions, providing a practical and reliable approach for post-fabrication resonance matching in material-integrated photonic devices. These results establish strain tuning as a promising strategy for overcoming spectral detuning and represent an important step toward the realization of tunable integrated nanophotonic platforms.[51–53].

4.5 Bibliography

1. A. Manna et al., "Cryo-Compatible In Situ Strain Tuning of 2D Material-Integrated Nanocavity," ACS Photonics, vol. 10, no. 9, pp. 3242–3247, Sep. 2023.

2. J. P. Reithmaier et al., "Strong coupling in a single quantum dot–semiconductor microcavity system," Nature, vol. 432, no. 7014, pp. 197–200, Nov. 2004

3. S. Noda, M. Fujita, and T. Asano, "Spontaneous-emission control by photonic crystals and nanocavities," Nature Photonics, vol. 1, no. 8, pp. 449–458, Aug. 2007, issn: 1749-4893.

4. H. Altug, D. Englund, and J. Vûckovíc, "Ultrafast photonic crystal nanocavity laser," Nature Physics, vol. 2, no. 7, pp. 484–488, Jul. 2006

5. S. Wu et al., "Monolayer semiconductor nanocavity lasers with ultralow thresholds," Nature, vol. 520, no. 7545, pp. 69–72, Apr. 2015, issn: 1476-4687.

6. J. Gu et al., "Enhanced nonlinear interaction of polaritons via excitonic Rydberg states in monolayer WSe2," Nature Communications, vol. 12, no. 1, p. 2269, Apr. 2021, issn: 2041-1723.

7. L. Zhang et al., "Van der Waals heterostructure polaritons with moiré-induced nonlinearity," Nature, vol. 591, no. 7848, pp. 61–65, Mar. 2021

8. T. Fryett, A. Zhan, and A. Majumdar, "Cavity nonlinear optics with layered materials," Nanophotonics, vol. 7, no. 2, pp. 355–370, Feb. 2018

9. K. Hennessy et al., "Quantum nature of a strongly coupled single quantum dot–cavity system," Nature, vol. 445, no. 7130, pp. 896–899, Feb. 2007

10. X. Liu et al., "Strong light–matter coupling in two-dimensional atomic crystals," Nature Photonics, vol. 9, no. 1, pp. 30–34, Jan. 2015

11. Y. Chen et al., "Deterministic Positioning of Colloidal Quantum Dots on Silicon Nitride Nanobeam Cavities," Nano Letters, vol. 18, no. 10, pp. 6404–6410, Oct. 2018

12. D. Rosser, T. Fryett, A. Saxena, A. Ryou, and A. Majumdar, "High-precision local transfer of van der Waals materials on nanophotonic structures," Optical Materials Express, vol. 10, no. 2, pp. 645–652, Feb. 2020,

13. A. Badolato et al., "Deterministic Coupling of Single Quantum Dots to Single Nanocavity Modes," Science, vol. 308, no. 5725, pp. 1158–1161, May 2005.

14. P. Lodahl, S. Mahmoodian, and S. Stobbe, "Interfacing single photons and single quantum dots with photonic nanostructures," Reviews of Modern Physics, vol. 87, no. 2, pp. 347–400, May 2015.

15. A. Sipahigil et al., "An integrated diamond nanophotonics platform for quantum-optical networks," Science, vol. 354, no. 6314, pp. 847–850, Nov. 2016.

16. K. Hennessy, A. Badolato, P. M. Petroff, and E. Hu, "Positioning photonic crystal cavities to single InAs quantum dots," Photonics and Nanostructures - Fundamentals and Applications, vol. 2, no. 2, pp. 65–72, Oct. 2004

17. E. Gil-Santos et al., "Scalable high-precision tuning of photonic resonators by resonant cavity-enhanced photoelectrochemical etching," Nature Communications, vol. 8, no. 1, p. 14 267, Jan. 2017

18. B. J. M. Hausmann et al., "Coupling of NV Centers to Photonic Crystal Nanobeams in Diamond," Nano Letters, vol. 13, no. 12, pp. 5791–5796, Dec. 2013

19. A. Faraon, D. Englund, I. Fushman, J.Vûcković, N. Stoltz,and P. Petroff, "Local quantum dot tuning on photonic crystal chips," Applied Physics Letters, vol. 90, no. 21, p. 213 110, May 2007

20. S. Sun, H. Kim, G. S. Solomon, and E. Waks, "Strain tuning of a quantum dot strongly coupled to a photonic crystal cavity," Applied Physics Letters, vol. 103, no. 15, p. 151 102, Oct. 2013

21. C. L. Yu et al., "Stretchable Photonic Crystal Cavity with Wide Frequency Tunability," Nano Letters, vol. 13, no. 1, pp. 248–252, Jan. 2013

22. T.-W. Lu, C.-C. Wu, C. Wang, and P.-T. Lee, "Compressible 1D photonic crystal nanolasers with wide wavelength tuning," Optics Letters, vol. 42, no. 12, pp. 2267–2270, Jun. 2017, issn: 1539-4794.

23. J.-H. Choi et al., "A high-resolution strain-gauge nanolaser," Nature Communications, vol. 7, no. 1, p. 11 569, May 2016, issn: 2041-1723.

24. B. T. Tung, D. V. Dao, T. Ikeda, Y. Kanamori, K. Hane, and S. Sugiyama, "Investigation of strain sensing effect in modified single-defect photonic crystal nanocavity," Optics Express, vol. 19, no. 9, pp. 8821–8829, Apr. 2011

25. K. F. Mak, C. Lee, J. Hone, J. Shan, and T. F. Heinz, "Atomically Thin MoS2: A New Direct-Gap Semiconductor," Physical Review Letters, vol. 105, no. 13, p. 136 805, Sep. 2010.

26. K. F. Mak and J. Shan, "Photonics and optoelectronics of 2D semiconductor transition metal dichalcogenides," Nature Photonics, vol. 10, no. 4, pp. 216–226, Apr. 2016, issn: 1749-4893.

27. C.-h. Liu, J. Zheng, Y. Chen, T. Fryett, and A. Majumdar, "Van der Waals materials integrated nanophotonic devices [Invited]," Optical Materials Express, vol. 9, no. 2, pp. 384–399, Feb. 2019

28. J. Pu et al., "Continuous Color-Tunable Light-Emitting Devices Based on Compositionally Graded Monolayer Transition Metal Dichalcogenide Alloys," Advanced Materials, vol. 34, no. 44, p. 2 203 250, 2022

29. Y. Li et al., "Room-temperature continuous-wave lasing from monolayer molybdenum ditelluride integrated with a silicon nanobeam cavity," Nature Nanotechnology, vol. 12, no. 10, pp. 987–992, Oct. 2017

30. I. Datta et al., "Low-loss composite photonic platform based on 2D semiconductor monolayers," Nature Photonics, vol. 14, no. 4, pp. 256–262, Apr. 2020

31. Q. Guo et al., "Black Phosphorus Mid-Infrared Photodetectors with High Gain," Nano Letters, vol. 16, no. 7, pp. 4648–4655, Jul. 2016

32. Q. Ma, G. Ren, A. Mitchell, and J. Z. Ou, "Recent advances on hybrid integration of 2D materials on integrated optics platforms," Nanophotonics, vol. 9, no. 8, pp. 2191–2214, Aug. 2020

33. P. Yin et al., "2D Materials for Nonlinear Photonics and Electro-Optical Applications," Advanced Materials Interfaces, vol. 8, no. 14, p. 2 100 367, 2021

34. H. Zhang et al., "Hybrid exciton-plasmon-polaritons in van der Waals semiconductor gratings," Nature Communications, vol. 11, no. 1, p. 3552, Jul. 2020

35. P. Kumar et al., "Light–matter coupling in large-area van der Waals superlattices," Nature Nanotechnology, vol. 17, no. 2, pp. 182–189, Feb. 2022

36. S. B. Anantharaman, K. Jo, and D. Jariwala, "Exciton–Photonics: From Fundamental Science to Applications," ACS Nano, vol. 15, no. 8, pp. 12 628–12 654, Aug. 2021, issn: 1936-0851

37. T. K. Fryett, Y. Chen, J. Whitehead, Z. M. Peycke, X. Xu, and A. Majumdar, "Encapsulated Silicon Nitride Nanobeam Cavity for Hybrid Nanophotonics," ACS Photonics, vol. 5, no. 6, pp. 2176–2181, Jun. 2018

38. T.-Y. Chang et al., "Black Phosphorus Mid-Infrared Light-Emitting Diodes Integrated with Silicon Photonic Waveguides," Nano Letters, vol. 20, no. 9, pp. 6824–6830, Sep. 2020, issn: 1530-6984.

39. D. Rosser, T. Fryett, A. Ryou, A. Saxena, and A. Majumdar, "Exciton–phonon interactions in nanocavity-integrated monolayer transition metal dichalcogenides," npj 2D Materials and Applications, vol. 4, no. 1, pp. 1–6, Jul. 2020

40. P. Rivera et al., "Coupling of photonic crystal cavity and interlayer exciton in heterobilayer of transition metal dichalcogenides," 2D Materials, vol. 7, no. 1, p. 015 027, Dec. 2019, issn: 2053-1583.

41. Y. K. Yogūrtçu, A. J. Miller, and G. A. Saunders, "Pressure dependence of elastic behaviour and force constants of GaP," Journal of Physics and Chemistry of Solids, vol. 42, no. 1, pp. 49–56, Jan. 1981

42. C. W. Hicks et al., "Strong Increase of Tc of Sr2RuO4 Under Both Tensile and Compressive Strain," Science, vol. 344, no. 6181, pp. 283–285, Apr. 2014.

43. J. Mutch et al., "Evidence for a strain-tuned topological phase transition in ZrTe5," Science Advances, vol. 5, no. 8, eaav9771, Aug. 2019.

44. C. W. Hicks, M. E. Barber, S. D. Edkins, D. O. Brodsky, and A. P. Mackenzie, "Piezoelectric-based apparatus for strain tuning," Review of Scientific Instruments, vol. 85, no. 6, p. 065 003, Jun. 2014

45. G. M. Diederich et al., "Tunable interaction between excitons and hybridized magnons in a layered semiconductor," Nature Nanotechnology, vol. 18, no. 1, pp. 23–28, Jan. 2023

46. J. Cenker et al., "Reversible strain-induced magnetic phase transition in a van der Waals magnet," Nature Nanotechnology, vol. 17, no. 3, pp. 256–261, Mar. 2022,

47. S. Chakravarthi et al., "Hybrid Integration of GaP Photonic Crystal Cavities with Silicon-Vacancy Centers in Diamond by Stamp-Transfer," Nano Letters, vol. 23, no. 9, pp. 3708–3715, May 2023

48. B. Aslan, M. Deng, and T. F. Heinz, "Strain tuning of excitons in monolayer WSe_2, Physical Review B, vol. 98, no. 11, p. 115 308, Sep. 2018.

49. O. A. Ajayi et al., "Approaching the intrinsic photoluminescence linewidth in transition metal dichalcogenide monolayers," 2D Materials, vol. 4, no. 3, p. 031 011, Jul. 2017

50. Q. Quan and M. Loncar, "Deterministic design of wavelength scale, ultra-high Q photonic crystal nanobeam cavities," Optics Express, vol. 19, no. 19, pp. 18 529–18 542, Sep. 2011

51. S. Ren, Q. Tan, and J. Zhang, "Review on the quantum emitters in two-dimensional materials," Journal of Semiconductors, vol. 40, no. 7, p. 071903, Jul. 2019

52. D. Huang, J. Choi, C.-K. Shih, and X. Li, "Excitons in semiconductor moiré superlattices," Nature Nanotechnology, vol. 17, no. 3, pp. 227–238, Mar. 2022

53. A. Javadi et al., "Single-photon non-linear optics with a quantum dot in a waveguide," Nature Communications, vol. 6, no. 1, p. 8655, Oct. 2015

54. S. G. Johnson, J. D. Joannopoulos, Block-Iterative Frequency-Domain Methods for Maxwell's Equations in a Planewave Basis. Opt. Express, OE 2001, 8 (3), 173–190.

55. Y. Yu, J. Cai, J. Sun, Z. Zhang, H. Qin, Fabrication and Characterization of a Wide-Bandgap and High-Q Terahertz Distributed-Bragg-Reflector Micro Cavities. Optics Communications 2018, 426, 84–88.

Chapter 5

Magnetically Tunable Coupling in CrSBr Integrated Nanocavities

This chapter contains contents from an unpublished manuscript currently in preparation. The text has been adapted for inclusion in this dissertation: Magnetically Tunable Coupling in CrSBr Integrated Nanophotonic Cavities **S. Pumulo**, A. Manna, A. Kala, H. Rarick, M. Nguyen, W. Li, D. G. Chica, X. Roy, X. Xu and A. Majumdar.

5.1 Abstract

Strong light–matter coupling is essential for quantum-enabled technologies, yet achieving precise spectral alignment in solid-state systems remains a challenge. While photonic crystal nanobeam cavities offer the necessary field confinement, fabrication-induced detuning often limits device performance. Here, we demonstrate magnetically tunable emitter-cavity coupling by integrating the 2D magnetic semiconductor CrSBr with gallium phosphide (GaP) nanobeam cavities. Leveraging CrSBr's exceptional magneto-optical response, we overcome initial spectral detuning to actively drive the system into resonance. We show that the intrinsic tunability of CrSBr allows for dynamic control of coupling strength and antenna-like effects between material excitations and confined cavity modes. These results establish the

CrSBr-nanobeam architecture as a versatile, reconfigurable platform for light–matter interactions, offering a robust pathway for developing tunable, integrated photonic components in future quantum architectures.

5.2 Introduction

Light–matter interactions form the foundation of photonics and underpin progress across a broad range of technologies, including optical communication, information storage, quantum information processing, integrated photonic circuits, spintronics, and other emerging platforms[1–4]. Enhancing the interaction between an optical emitter and a resonant cavity is central to many of these applications[5–7] and is fundamentally governed by the degree of electromagnetic field confinement. In particular, reducing the optical mode volume concentrates the field intensity, thereby significantly increasing the interaction strength between confined optical modes and material excitations.

Over the past several decades, advances in photonic crystal cavities (PhCC) have enabled the systematic realization of ultra-small mode volumes through highly controlled and scalable design methodologies[8,9]. These structures provide a versatile platform for engineering cavity resonances and tailoring spatial field distributions, making them ideally suited for studying and exploiting enhanced emitter–cavity interactions. One result of this enhanced field confinement is the optical antenna effect[34,35], a phenomenon that occurs when an electromagnetic field is concentrated into a small volume resulting in an enhancement of spectral emission and modification in properties such as directionality and polarization of a coupled emitter. Consequently, extensive efforts have been devoted to coupling a wide variety of emitters to PhCCs, ranging from quantum dots and color centers to atomic and molecular systems[10–15].

Recently, the emergence of two-dimensional (2D) materials has introduced new opportunities

for hybrid light-matter platforms[16–20]. Unlike conventional bulk or epitaxial emitters, 2D materials circumvent lattice-matching constraints while hosting a diverse range of strongly confined excited states that are intrinsically compatible with nanoscale photonic environments. Additionally, their optical and electronic properties can be dynamically tuned through multiple external degrees of freedom, including electrostatic gating, strain, and environmental control[36–38]. These attributes position 2D materials as a uniquely flexible class of emitters for integration with PhCCs.

Despite the potential of 2D material integrated PhCCs, several challenges remain. In particular, the transfer of either the emitter onto the cavity or vice versa often introduces spectral detuning between the optical resonance and the material excitation, thereby limiting effective coupling between the system components. Although tuning of the cavity resonance has been explored as a strategy to overcome this often-occurring mismatch, such approaches frequently lack reversibility[21–23], perturb the surrounding photonic environment and can compromise cavity performance[24–29].

An effective alternate strategy is to instead reversibly and continuously tune the emitter resonance directly and exclusively. In this work, we adopt this approach by exploiting the properties of the van der Waals antiferromagnet CrSBr. This 2D material hosts a rich set of functionalities, among which its pronounced magneto-optical response is of central importance here, providing a non-invasive and reversible tuning mechanism 28-30. While the high refractive index of CrSBr[31] presents additional challenges for integration with PhCCs, requiring careful control to avoid unintended resonance shifts, we mitigate these effects by using a thin CrSBr flake.

Using this approach, we demonstrate coupling between CrSBr excitations and a GaP nanobeam cavity (NB), a one-dimensional PhCC an ultra-small mode volume. This coupled emission shows 1.4 times enhancements in photoluminescence as well as coupled polarization directionality supporting a hypothesis of optical antenna effect. Furthermore, we show reversible

tuning of the CrSBr emitter resonance, enabling controlled coupling into and out of resonance with the cavity mode, even in conditions where the spectral detuning is 2.5 nm. These results highlight the potential of magnetically tunable, all-dielectric hybrid nanophotonic platforms and establish a pathway toward reconfigurable photonic devices based on 2D materials.

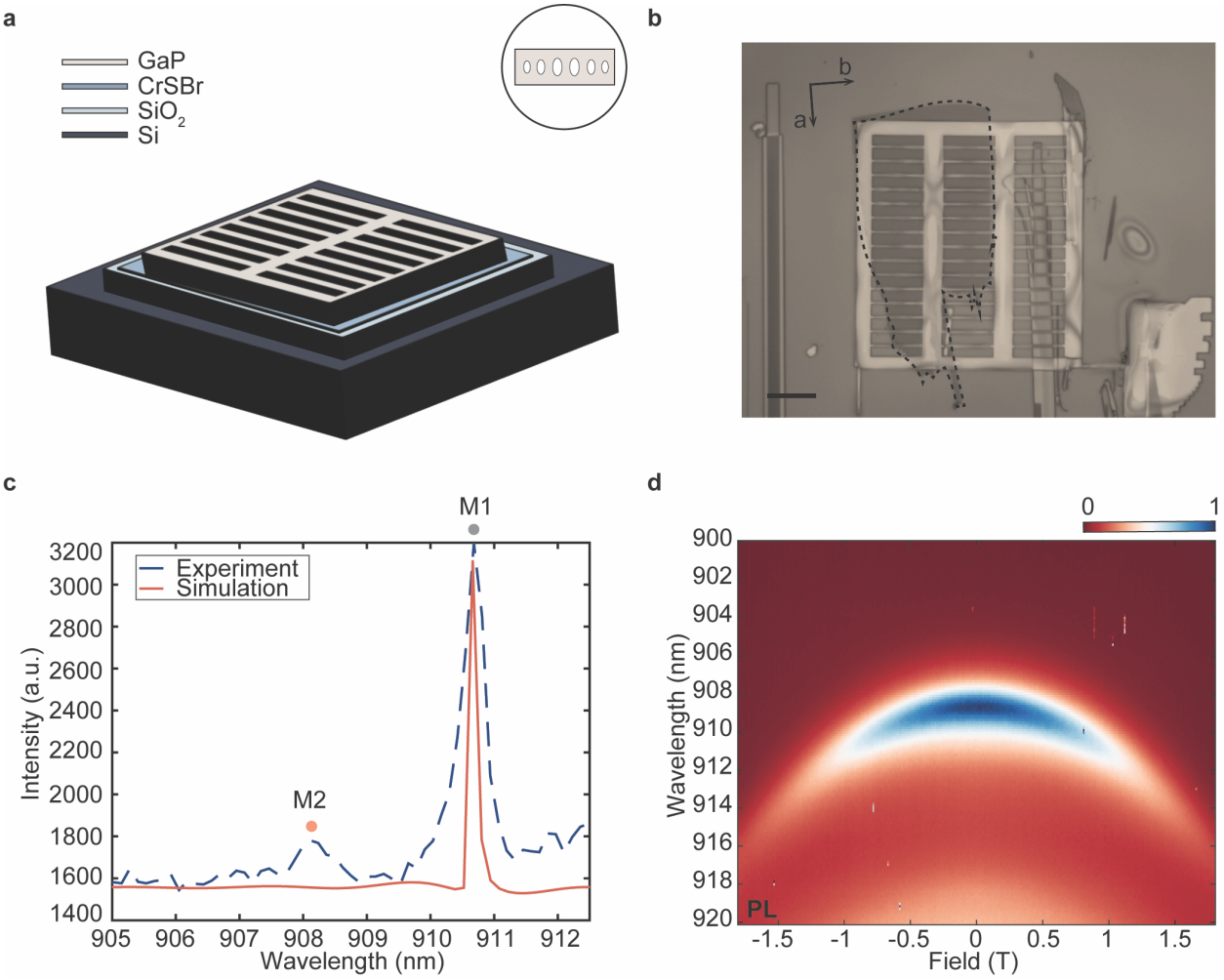

Figure 5.2.1: (a) Schematic illustration of the CrSBr-nanobeam coupled system on a 285 nm SiO_2/Si substrate with the inset illustrating a zoom in of the nanobeam (b) Optical image of the CrSBr-nanobeam coupled system on a 285 nm SiO_2/Si substrate with the dashed outline representing the CrSBr flake (scale bar: 5 μm) (c) Simulated GaP nanobeam cavity mode and experimentally acquired photoluminescence spectrum of a GaP nanobeam cavity modes (M1 and M2). (d) Normalized in-plane magnetic field dependent photoluminescence of a CrSBr flake measured at 4 K.

5.3 Results

CrSBr hosts strongly anisotropic in-plane excitonic transitions and exhibits a relatively high refractive index, both of which impose important constraints on its integration with optical cavities. To achieve efficient coupling while preserving the cavity resonance, careful consideration must be given to both the crystallographic orientation of the material relative to the cavity field polarization and the geometric dimensions of the CrSBr flake. In particular, excessive index mismatch between CrSBr and the GaP cavity can lead to substantial resonance shifts or complete disappearance of the cavity mode if not properly managed.

The device fabrication process begins with the deposition of CrSBr flakes onto a 285 nm SiO_2/Si substrate using a mechanical exfoliation technique. In this process, bulk CrSBr crystals are cleaved using adhesive tape and subsequently transferred onto the substrate, where thinner flakes adhere preferentially via van der Waals interactions. Following exfoliation, optical microscopy is employed to identify and select flakes of suitable thickness and lateral dimensions for device fabrication. To mitigate perturbations to the cavity resonance from the index contrast, a 4 nm thin CrSBr flake is used in this study. The next step is enabled by recent advancements in nanobeam (NB) cavity fabrication, realizing transferable cavity arrays, allowing the photonic structure to be deterministically placed directly onto a target material flake as illustrated schematically in Fig. 1a. This is accomplished using established van der Waals transfer techniques, which enable controlled alignment between the cavity mode polarization and the anisotropic optical axes of CrSBr (identified optically through its long and short crystal directions). The result of this is transfer is captured optically in Figure 1b.

In Figure 1c the electromagnetically simulated spectrum of a NB mode is compared to the photoluminescence (PL) measurements of a representative nanobeam cavity array, revealing that in the spectral region of interest, the experimental NB exhibits two distinct cavity modes, mode 1 (M1) which matches our simulated mode and an additional mode we will

refer to as mode 2 (M2). Because of its relatively stronger coupling to the material emission, M1 will be the focus of the discussion.

In order to have a reference for the uncoupled flake emission, we measured the in-plane magnetic field dependent PL of the CrSBr exciton at 4K, revealing its characteristic magneto-optical coupling. As the applied magnetic field is increased from 0 T to 1.5 T, the exciton emission undergoes a spectral shift of approximately 10 nm (Fig. 1d) highlighting the suitability of CrSBr as an actively tunable emitter for hybrid nanophotonic systems. This same flake is what is used for the rest of the study.

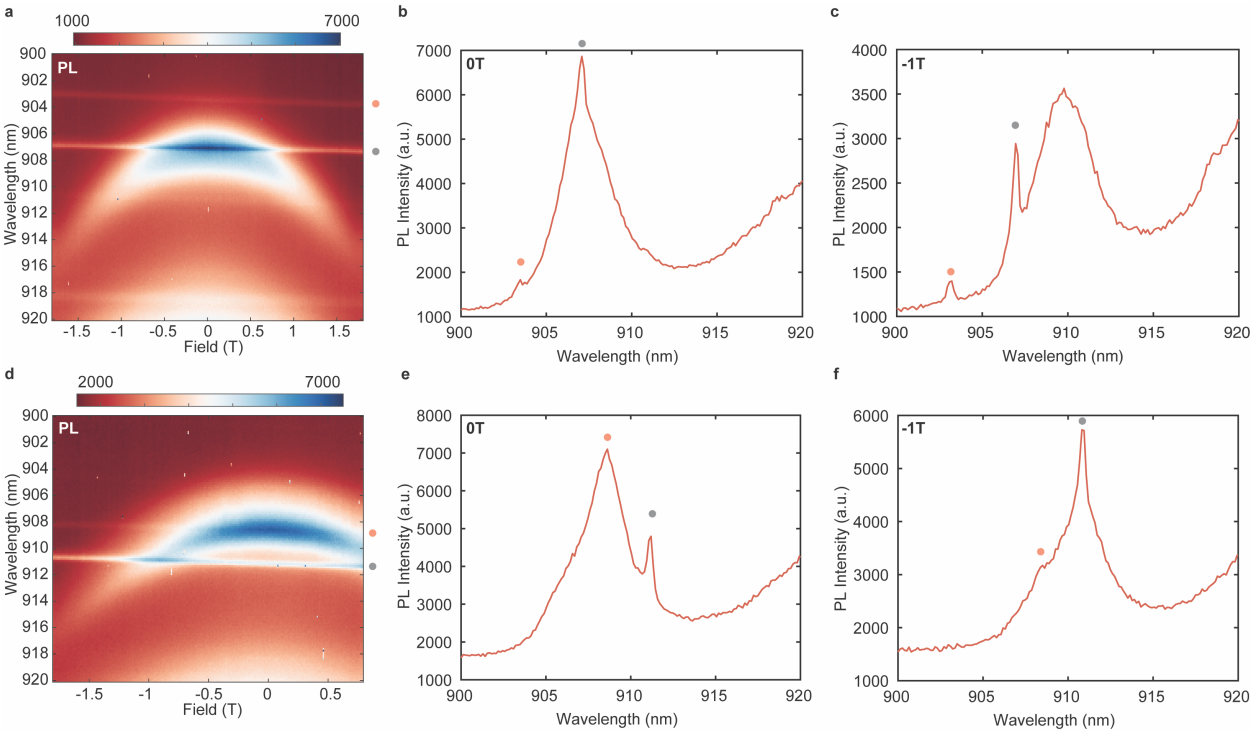

Figure 5.3.1: (a) Magnetic field dependent PL of Device 1 (D1) showing coupling between the CrSBr emitter and the nanobeam cavity mode, where the grey and red dots represent the modes M1 and M2 respectively (b) PL of D1 at 0 T highlighting emitter-cavity coupling (c) PL of D1 at -1 T showing decoupling between the cavity mode and the emitter (d) Magnetic field dependent PL of Device 2 (D2) demonstrating reversible tuning of the emitter into and out of resonance with the cavity mode (e) PL of D2 at 0 T where the emitter is detuned from the cavity mode (f) PL of D2 at 1 T showing emitter-cavity coupling.

The initial step in investigating coupling between the NBs and the CrSBr flake is to satisfy the

spectral matching condition in the absence of external tuning. This is achieved by selecting NBs whose resonant modes are intrinsically aligned with the CrSBr exciton emission using PL. For Device 1 as shown in Fig. 2a, at zero applied magnetic field (0 T) the CrSBr emission is spectrally matched to the cavity resonance of mode 1 (M1), resulting in a modest enhancement of the photoluminescence intensity. This effect is attributable to emitter–cavity coupling, hinting towards optical antenna effect.

From Device 1, we directly observe coupling between the CrSBr emission and the cavity mode, demonstrating the viability of this platform despite the constraints arising from the large refractive index of the material. Furthermore, magnetic field dependent measurements reveal reversible tuning of the excitonic resonance, and consequently of the emitter–cavity coupling. Although the effect in Device 1 is limited by the fact that the system is already at resonance at 0 T, this tuning mechanism is particularly valuable for NB-CrSBr devices that are spectrally detuned at zero field.

One such device exhibiting spectrally detuned M1 and emitter resonances at 0 T is Device 2, where the cavity mode and the CrSBr emission peak are separated by approximately 2.5 nm (Fig. 2d). In the absence of active tunability, this level of detuning would severely limit the ability to explore emitter-cavity coupling. However, the intrinsic magnet-optical coupling of CrSBr provides a pathway to overcome this constraint. As shown in Fig. 2c, the system evolves from maximal detuning at 0 T to clear spectral overlap and observable coupling at magnetic fields near -1 T, which is highlighted in Fig. 2e and Fig. 2f.

Importantly, this behavior demonstrates not only that an initially nonresonant system can be tuned into resonance, but also that the tuning process is fully reversible and does not induce observable degradation of either the material or the cavity. This stands in contrast to mechanical tuning approaches, which can introduce irreversible strain or long-term device instability. The ability to reversibly tune into resonance relaxes the stringent spectral matching requirements typically imposed on NB-emitter systems, enabling broader device

yield and greater flexibility in integrating CrSBr with nanophotonic structures.

These results clearly demonstrate emitter-cavity coupling and reversible magnetic field induced tuning in both Device 1 and 2. Additionally, from the spectral overlap of the devices, we estimate an emission enhancement factor of approximately 1.4 times in both Device 1 and Device 2: providing again a basis for the argument of the optical antenna effect. This enhancement value is determined by first obtaining the uncoupled emitter intensity, I_{CrSBr}. This is the compared to the emitter-cavity intensity measured under resonant conditions, $I_{CrSBr+NB}$. The enhancement factor is then calculated as $I_{CrSBr+NB}$ / I_{CrSBr}.

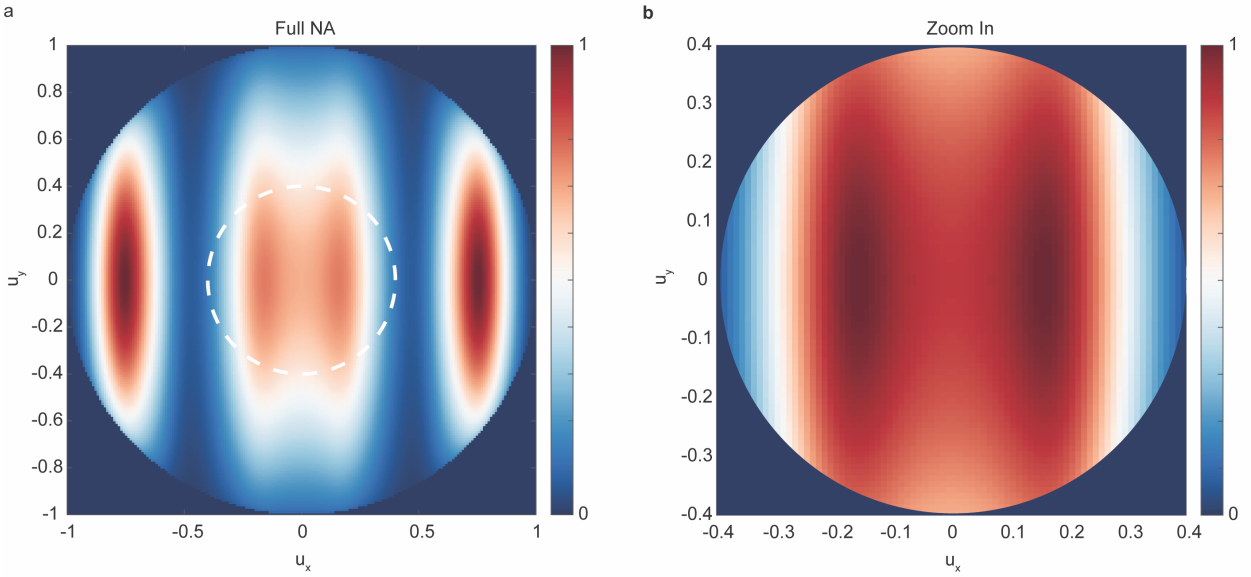

Figure 5.3.2: (a) Simulated normalized far-field pattern of the M1 mode of the nanobeam cavity. The white dash circle represents a numerical aperture (NA) of 0.4 which matches the experimental PL measurement (b) Zoomed in image of (a) and renormalized within the desired NA.

The simulated far-field emission profile of the cavity mode is shown in Fig. 3. Within a collection numerical aperture of NA = 0.4, the cavity mode exhibits a collection efficiency of $\eta_{|cavity}$=26% (further analysis is included in the Methods section). Under the same collection conditions, an in-plane dipole yields a collection efficiency of $\eta_{|dipole}$=16%. The resulting ratio, $\eta_{|cavity}/\eta_{|dipole} = 1.6$, represents the theoretical enhancement in collected emission arising from the cavity-modified radiation pattern. This predicted enhancement is in good agreement with

the experimentally measured value, providing further evidence that the observed increase in collected photoluminescence originates from the cavity's optical antenna effect.

These findings establish a proof of concept for magnetically tunable hybrid NB-CrSBr systems and underscore their potential for applications in light-matter interaction studies and reconfigurable nanophotonic devices.

It should be noted that a consistent blueshift of approximately 2 nm is observed in the exciton PL when comparing the bare CrSBr flake (Fig. 1d) to the cavity-coupled regime (Fig. 2a and d). This shift is attributable to strain induced by the placement of the GaP NB directly on top of the CrSBr flake, which can modify the excitonic energy through lattice deformation. This however does not change any of the observable scienceobserved cavity-exciton coupling.

In order to prove optical antenna effect, linear polarization needs to be probed, another critical factor governing the coupling between these linearly polarized NBs and CrSBr. Both the CrSBr emitter and the cavity exhibit strongly anisotropic polarization responses, as shown in Fig. 3c and Fig. 3d, respectively, necessitating careful consideration of the relative angular alignment between the two components. However, the same figures also highlight a measurable offset between the preferential polarization axis of the cavity and that of the CrSBr flake resulting from the deviations in cavity design and slight misalignment during the transfer process.

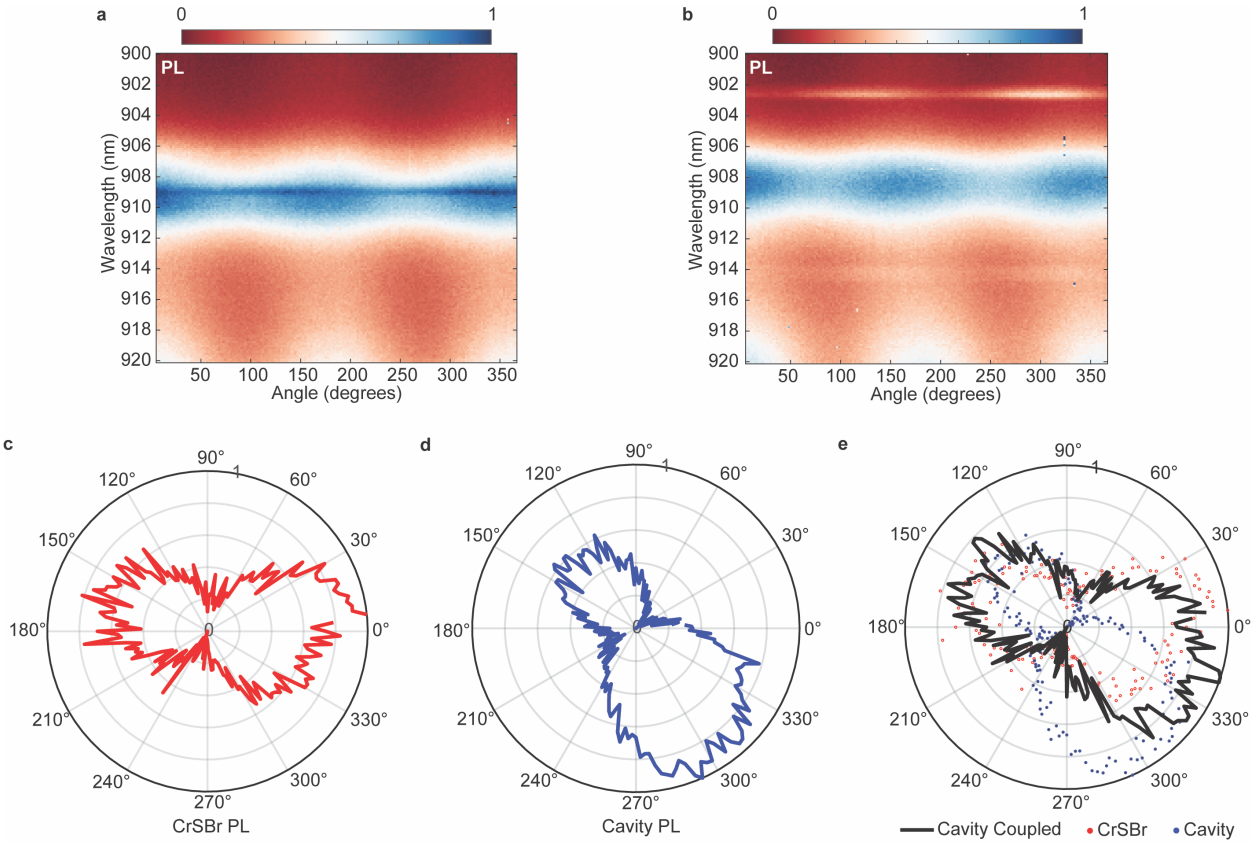

Figure 5.3.3: Normalized polarization-dependent photoluminescence (PL) of Device 3 (D3) where the CrSBr emitter and cavity mode are spectrally detuned (b) Normalized polarization dependent PL of Device 4 (D4) exhibiting emitter-cavity coupling (c) Polar plot of the polarization dependent PL from a CrSBr flake (d) Polar plot of the polarization resolved PL from the nanobeam cavity (e) Polar plot of the polarization-resolved PL from the coupled CrSBr-cavity device.

Figure 3a presents the polarization dependent PL of an uncoupled CrSBr-NB system, where the maxima of the emission intensities occur at distinct polarization angles, reflecting the aforementioned angular mismatch. In contrast, under coupled conditions (Fig. 3b), the PL intensity reaches a maximum at an intermediate polarization angle corresponding to optimal overlap between the cavity mode and the CrSBr emission. Extracting and comparing the polarization dependent intensities reveals a clear intersection point in the coupled device, indicating that the preferential polarization of the hybrid system lies between those of the individual cavity and emitter.

This polarization hybridization provides additional evidence of emitter-cavity coupling and

the antenna effect, as the coupled system inherits characteristics from both constituent components. Although future work will aim to minimize polarization mismatch through improved alignment and cavity design, the observed PL enhancement, polarization hybridization, and strong dependence on spectral and angular alignment are all consistent with an antenna-mediated interaction. In this picture, the NB concentrates the optical field and reshapes the radiation characteristics of the CrSBr excitons, while magnetic-field tuning provides a dynamic mechanism to control the spectral overlap between the emitter and the antenna resonance. This establishes CrSBr-NB devices as magnetically tunable dielectric optical antennas, offering a route toward actively reconfigurable nanoscale light sources.

5.4 Conclusion

In summary, we demonstrate magnetically tunable coupling between CrSBr and GaP nanobeam photonic crystal cavities, establishing a platform for controllable light-matter interactions. By exploiting the intrinsic magneto-optical coupling of CrSBr, we achieve reversible tuning of the excitonic emission into and out of resonance with cavity modes, enabling coupling even in initially spectrally detuned systems. Despite challenges associated with the high refractive index and strong anisotropy of CrSBr, careful control of flake thickness and device alignment allows for observable PL enhancement under coupled conditions.

Polarization dependent measurements further reveal hybridization between the anisotropic emission of CrSBr and the cavity mode, providing additional evidence of coupling even with angular misalignment. The observed reversible tuning, enhancement factors, and robustness against mechanical degradation highlight the advantages of magnetic field-based control over conventional tuning approaches.

Beyond the cavity electrodynamics perspective, the nanobeam cavity can also be understood as operating in the regime of a dielectric optical antenna. In this weak-coupling regime, the

cavity does not form hybrid light–matter states but instead modifies the local photonic density of states, enhancing and directing emission from nearby excitons.

Together, these results relax stringent spectral matching requirements and underscore the potential of CrSBr-integrated nanophotonic devices for reconfigurable coupled light–matter platforms and future integrated photonic technologies. Particularly, with improved coupling between the cavities and excitons of CrSBr and precise alignment, this method could be used in the determination of strong coupling in nondispersive photonic crystal cavities via observable anti-crossings in magneto photoluminescence spectra.

5.5 Methods

5.5.1 Nanobeam Design

The design the nanobeam cavity we utilized the design approach established in a previous report1. To design the nanobeam cavity, we first simulated the band diagram using MIT Photonic Bands (MPB). Following this the cavity was optimized in Ansys Lumerical FDTD using the quality factor as the figure of merit. The design system consists of 215 nm thick and 393 nm wide GaP film on a silicon substrate. The light confinement is done by 10 elliptical holes that taper in size with reflectors that are composed of 15 Bragg mirror holes.

5.5.2 Fabrication

The fabrication process follows procedures similar to those reported previously 2. CrSBr flakes are first mechanically exfoliated onto a 285 nm SiO_2/Si substrate. Optical microscopy is used to locate candidate flakes, after which atomic force microscopy (AFM) measurements determine flake thickness. Thin flakes suitable for integration are subsequently optically characterized.

Nanobeam (NB) cavities are fabricated from a 215 nm thick GaP membrane grown on silicon via chemical vapor deposition (CVD) and obtained from the vendor, NAsP III/V GmbH. A section of the wafer is spin-coated with approximately 400 nm of ZEP520A resist and patterned using a 100 kV JEOL JBX6300FX electron-beam lithography system. The pattern is transferred into the GaP layer through reactive ion etching (RIE) using a Cl_2/Ar chemistry. The nanobeams are then released by selectively removing the underlying silicon using vapor-phase xenon difluoride (XeF_2) etching, which provides a stiction-free and residue-free process, allowing suspension of the fragile structures without mechanical damage.

Following fabrication, the NB cavities are optically characterized, and structures with resonances closest to the CrSBr PL maximum are selected. These cavities are subsequently transferred onto the CrSBr flakes using a standard dry van der Waals transfer technique as seen in SF1.

5.5.3 Optical Measurements

Optical measurements were carried out using a closed-cycle helium cryostat (Opticool by Quantum Design) with most sample measurements taken at a temperature of 4 K. For PL measurements, a 632.8 nm He-Ne laser was focused to a 1 μm spot at a power of 20 μW using a microscope objective. The emitted signal was spectrally dispersed with a grating spectrometer and detected by a liquid-nitrogen-cooled charge-coupled device (CCD), with a minimum of three frames acquired per measurement.

5.5.4 Antenna Effect Calculation

The far-field emission profiles of both the cavity mode and an in-plane dipole were simulated using Lumerical FDTD. The collection efficiency into a specified NA is defined as the fraction of the total radiated power captured within the collection cone,

where the numerator represents the far-field intensity integrated over the angular range

corresponding to the collection NA, and the denominator represents the total radiated far-field intensity.

5.6 Supplementary Information

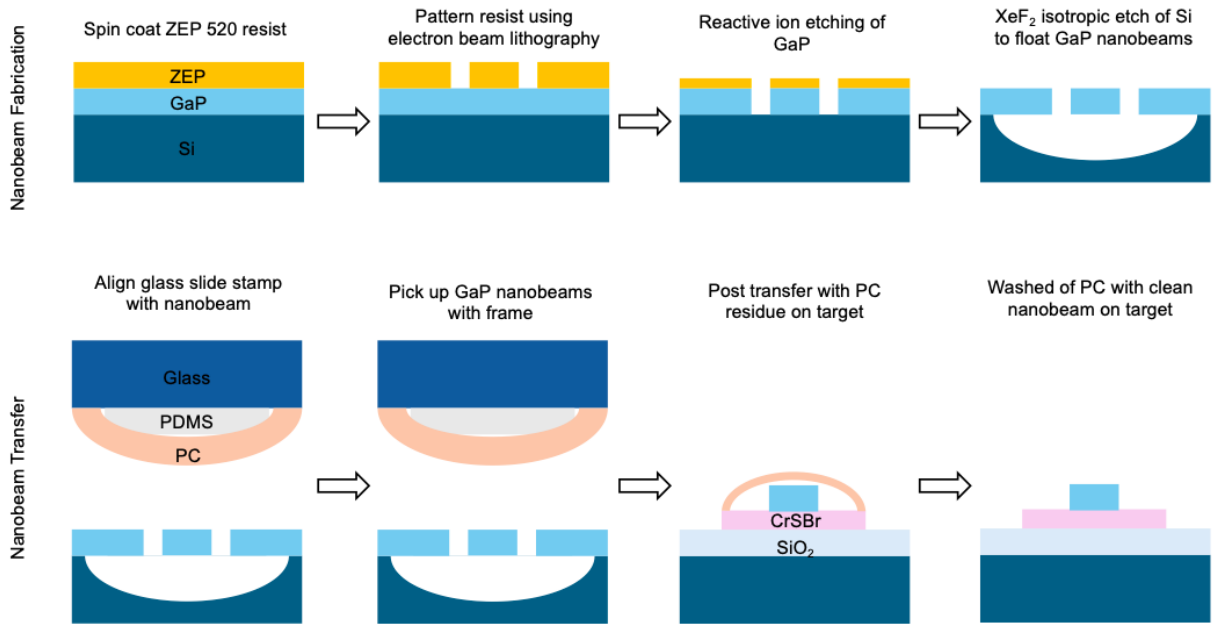

Figure 5.6.1: Illustration of the nanobeam fabrication and transfer processes.

5.7 Bibliography

1. Reithmaier, J. P. et al. Strong coupling in a single quantum dot–semiconductor microcavity system. Nature 432, 197–200 (2004).

2. González-Tudela, A., Reiserer, A., García-Ripoll, J. J. et al. Light–matter interactions in quantum nanophotonic devices. Nat. Rev. Phys. 6, 166–179 (2024).

3. Rivera, N. & Kaminer, I. Light–matter interactions with photonic quasiparticles. Nat. Rev. Phys. 2, 538–561 (2020).

4. Wang, J., Sciarrino, F., Laing, A. et al. Integrated photonic quantum technologies. Nat. Photon. 14, 273–284 (2020).

5. Noda, S., Fujita, M. & Asano, T. Spontaneous-emission control by photonic crystals and nanocavities. Nat. Photon. 1, 449–458 (2007).

6. Altug, H., Englund, D. & Vučković, J. Ultrafast photonic crystal nanocavity laser. Nat. Phys. 2, 484–488 (2006).

7. Wu, S. et al. Monolayer semiconductor nanocavity lasers with ultralow thresholds. Nature 520, 69–72 (2015).

8. Miura, R. et al. Ultralow mode-volume photonic crystal nanobeam cavities for high-efficiency coupling to individual carbon nanotube emitters. Nat. Commun. 5, 5580 (2014).

9. Majumdar, A. et al. Quantum optics with single quantum dots in photonic crystal cavities. In Quantum Optics with Semiconductor Nanostructures (ed. Jahnke, F.) 46–78 (Woodhead Publishing, 2012).

10. Ding, S. W. et al. High-Q cavity interface for color centers in thin-film diamond. Nat. Commun. 15, 6358 (2024).

11. Chen, Y. et al. Deterministic positioning of colloidal quantum dots on silicon nitride nanobeam cavities. Nano Lett.18, 6404–6410 (2018).

12. Badolato, A. et al. Deterministic coupling of single quantum dots to single nanocavity modes. Science 308, 1158–1161 (2005).

13. Lodahl, P., Mahmoodian, S. Stobbe, S. Interfacing single photons and single quantum dots with photonic nanostructures. Rev. Mod. Phys. 87, 347–400 (2015).

14. Sipahigil, A. et al. An integrated diamond nanophotonics platform for quantum-optical networks. Science 354, 847–850 (2016).

15. Hennessy, K., Badolato, A., Petroff, P. M. Hu, E. Positioning photonic crystal cavities to single InAs quantum dots. Photon. Nanostruct. Fundam. Appl. 2, 65–72 (2004).

16. Rosser, D., Fryett, T., Saxena, A., Ryou, A. Majumdar, A. High-precision local transfer of van der Waals materials on nanophotonic structures. Opt. Mater. Express 10, 645–652 (2020).

17. Liu, C.-H., Zheng, J., Chen, Y., Fryett, T. Majumdar, A. Van der Waals materials integrated nanophotonic devices. Opt. Mater. Express 9, 384–399 (2019).

18. Pu, J. et al. Continuous color-tunable light-emitting devices based on compositionally graded monolayer transition metal dichalcogenide alloys. Adv. Mater. 34, 2203250 (2022).

19. Li, Y. et al. Room-temperature continuous-wave lasing from monolayer molybdenum ditelluride integrated with a silicon nanobeam cavity. Nat. Nanotechnol. 12, 987–992 (2017).

20. Datta, I. et al. Low-loss composite photonic platform based on 2D semiconductor monolayers. Nat. Photon. 14, 256–262 (2020).

21. Gil-Santos, E. et al. Scalable high-precision tuning of photonic resonators by resonant cavity-enhanced photoelectrochemical etching. Nat. Commun. 8, 14267 (2017).

22. Hausmann, B. J. M. et al. Coupling of NV centers to photonic crystal nanobeams in diamond. Nano Lett. 13, 5791–5796 (2013).

23. Faraon, A., Englund, D., Fushman, I., Vučković, J., Stoltz, N. Petroff, P. Local quantum dot tuning on photonic crystal chips. Appl. Phys. Lett. 90, 213110 (2007).

24. Sun, S., Kim, H., Solomon, G. S. Waks, E. Strain tuning of a quantum dot strongly coupled to a photonic crystal cavity. Appl. Phys. Lett. 103, 151102 (2013).

25. Yu, C. L. et al. Stretchable photonic crystal cavity with wide frequency tunability. Nano Lett. 13, 248–252 (2013).

26. Lu, T.-W., Wu, C.-C., Wang, C. & Lee, P.-T. Compressible 1D photonic crystal nanolasers with wide wavelength tuning. Opt. Lett. 42, 2267–2270 (2017).

27. Manna, A. et al. Cryo-compatible in situ strain tuning of 2D material-integrated nanocavity. ACS Photonics 10, (2023).

28. Wilson, N. P. et al. Interlayer electronic coupling on demand in a 2D magnetic semiconductor. Nat. Mater. 20, 1657–1662 (2021).

29. Lee, K. et al. Magnetic order and symmetry in the 2D semiconductor CrSBr. Nano Lett. 21, 3511–3517 (2021).

30. Göser, O., Paul, W. & Kahle, H. Magnetic properties of CrSBr. J. Magn. Magn. Mater. 92, 129–136 (1990).

31. Wang, T. et al. Magnetically dressed CrSBr exciton-polaritons in ultrastrong coupling regime. Nat. Commun. 14, 5966 (2023).

32. Demir, A. K. et al. Tunable nanophotonic devices and cavities based on a two-dimensional magnet. Nat. Photonics(2025).

33. Dirnberger, F. et al. Magneto-optics in a van der Waals magnet tuned by self-hybridized polaritons. Nature 620, 533–537 (2023).

34. Novotny, L., van Hulst, N. Antennas for light. Nature Photon 5, 83–90 (2011).

35. Córdova-Castro, R.M., van Dam, B., Lauri, A. et al. Single-emitter super-resolved imaging of radiative decay rate enhancement in dielectric gap nanoantennas. Light Sci Appl 13, 7 (2024).

36. Mak, K., Shan, J. Photonics and optoelectronics of 2D semiconductor transition metal dichalcogenides. Nature Photon 10, 216–226 (2016).

37. Wugang Liao, Yanting Huang, Huide Wang, Han Zhang, Van der Waals heterostructures for optoelectronics: Progress and prospects, Applied Materials Today, Volume 16, 2019, Pages 435-455

38. Eunice Paik, Long Zhang, Kin Fai Mak, Jie Shan, and Hui Deng, "Excitons and polaritons in two-dimensional transition metal dichalcogenides: a tutorial," Adv. Opt. Photon. 16, 1064-1132 (2024)

Chapter 6

Outlook

This dissertation demonstrates three complementary approaches for engineering light-matter interactions in low-dimensional material-integrated nanophotonic systems through spatial confinement, mechanical strain, and magnetism. Together, these tuning mechanisms address one of the principal challenges in integrated photonics: achieving reliable and controllable resonance matching between optical cavities and low-dimensional materials.

First, we showed that geometric engineering in the weak-confinement regime enables systematic tuning of the CrSBr exciton resonance. When combined with the material's intrinsic self-hybridized EP states, mesoscopic CrSBr structures exhibit size-dependent quantized EP resonances while preserving the defining optical and magneto-optical properties of the parent thin film. The ability to tune these EP resonances through both spatial confinement and magnetic field demonstrates a unique multidimensional control platform, where structural and magnetic degrees of freedom can be independently or simultaneously exploited to engineer hybrid light-matter states.

Second, we demonstrated reversible strain tuning of a PCC over a wavelength range of approximately 5 nm while maintaining minimal degradation of the cavity quality factor. This tuning remained effective under cryogenic conditions, providing a practical post-fabrication

approach for compensating spectral detuning and enabling reliable resonance matching in material-integrated photonic devices. These results establish strain as an effective means of dynamically controlling cavity resonances without compromising device performance.

Finally, we demonstrated reversible, nondestructive magnetic tuning of the coupling between CrSBr and GaP nanobeam PCCs. By exploiting the intrinsic magneto-optical response of CrSBr, excitonic emission could be tuned into and out of resonance with the cavity mode, enabling controllable coupling even in devices that were initially spectrally detuned. Despite the challenges associated with the high refractive index and strong optical anisotropy of CrSBr, careful optimization of flake thickness and device alignment enabled measurable cavity-enhanced PL, establishing magnetic tuning as a versatile alternative to mechanical approaches.

Together, these results demonstrate that resonance tuning in integrated nanophotonic systems need not rely on a single external stimulus. Instead, structural confinement, mechanical deformation, and intrinsic magnetic ordering provide complementary mechanisms for dynamically engineering light-matter interactions across multiple length scales. Looking forward, the combination of these tuning strategies with increasingly sophisticated nanophotonic architectures could enable actively reconfigurable photonic devices, deterministic control of polaritonic states, and robust cavity-coupled quantum emitters. More broadly, extending these concepts to emerging low-dimensional materials and complex VdW heterostructures may provide new opportunities to explore hybrid quantum systems, strongly correlated polaritonic phases, and multifunctional photonic devices in which optical, mechanical, and magnetic degrees of freedom can be engineered simultaneously.